Review paper

A review of the high-entropy ceramic materials for thermal barrier coatings: Design, synthesis, sintering and properties

Jiahang Liu[1], Yiyong Wang[1], Zhe Lu[1,*], Yanwen Zhou[1], Yan Li[1], Jing Zhang[2], Guanlin Lyu[3], Yeon-Gil Jung[4]

[1]*School of Materials and Metallurgical Engineering, University of Science and Technology Liaoning, Anshan 114051, China*

[2]*State Department of Mechanical and Energy Engineering, Indiana University - Purdue University, Indianapolis, IN 46202-5132, USA*

[3]*Key Lab of New Ceramics and Fine Processing, School of Materials Science and Engineering, Tsinghua University, Beijing 100084, China*

[4]*School of Materials Science and Engineering, Changwon National University, Changwon, Gyeongnam 641-773, Republic of Korea*

Received 21 October 2024; received in revised form 7 February 2025; accepted 23 February 2025

Abstract

Thermal barrier coatings are used as a surface technology for hot-end components of turbine engines, and the continuous development of aerospace technology puts higher requirements on ceramic materials for thermal barrier coatings. High-entropy ceramics, as a novel material developed recently, have received wide attention due to their particular structure and high-entropy effect. In recent years, researchers have shown interest in various high-entropy ceramics due to their exceptional thermodynamic properties and outstanding thermal insulation capabilities. These ceramics are being considered for potential application in thermal barrier coatings. This paper reviews the component design theory, synthesis methods, sintering methods and functional performance of high-entropy ceramics for thermal barrier coatings. The future development direction of high-entropy ceramics for thermal barrier coatings is also prospected.

Keywords*: thermal barrier coatings, high-entropy ceramics, component design, fabrication, properties*

Contents

1. Introduction....1
2. High-entropy ceramic composition design....2
3. Synthesis of high-entropy oxide powders....4
3.1 Solid-state reaction....5
3.2 Sol-gel method....5
3.3 Co-precipitation method....6
3.4 Solution combustion method....7
4. Fabrication of TBCs with high-entropy oxides....8
5. Sintering of high-entropy ceramics....8
5.1 Common sintering....9
5.2 Ultra-fast high-temperature sintering....9
5.3 Spark plasma sintering....11
5.4 Flash sintering....12
6. Properties of high-entropy ceramics....13
6.1 Thermal conductivity....13
6.2 Fracture toughness....15
6.3 Coefficient of thermal expansion....16
6.4 Anti-sintering properties....17
6.5 Anti-corrosion properties....18
6.6 High-temperature phase stability....20
6.7 Chemical compatibility....20
7. Summary and outlook....21
References....22

*Corresponding author: tel: +86 17695663005
e-mail: *lz19870522@126.com*

I. Introduction

With the continuous development of aerospace technology, the engine's inlet temperature is projected to reach 2100 K as efforts are made to enhance the output power of gas turbines and the thrust-weight ratio of turbine engines [1]. For the engine's internal nozzles, blades, combustion chambers and other hot-end components, the commonly used base material is a nickel-based high-temperature alloy, with an operating temperature of ~1075 °C, which is far lower than the

engine front inlet temperature [2]. In the 1950s, NASA proposed the concept of thermal barrier coatings to make turbine engines suitable for higher-temperature operating environments. With the continuous development of preparation methods and material selection, a significant breakthrough was achieved in the early 1980s [3].

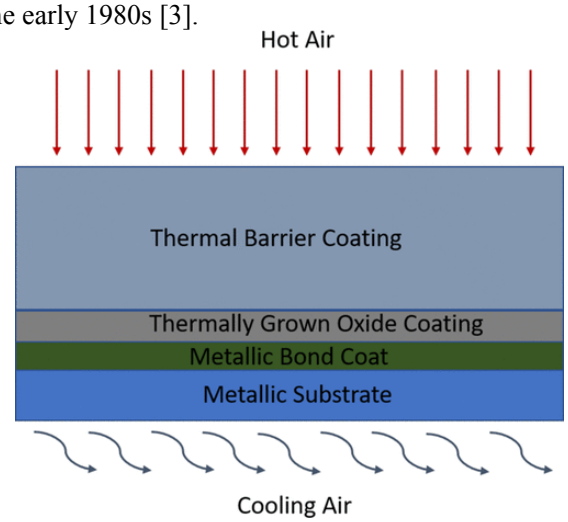

Figure 1. Schematic of a traditional TBC design [4]

Thermal barrier coatings (TBCs) are sophisticated multilayer coatings that offer thermal insulation and lower the surface temperature of hot-end components in aerospace engines. Traditional TBCs typically consist of four components (Fig. 1): i) a high-temperature resistant nickel-based or cobalt-based alloy substrate, ii) a metal bond coat (BC) with exceptional high-temperature oxidation resistance, iii) a thermally grown oxide (TGO) layer formed in a high-temperature environment and iv) a ceramic top coat (TC) [4–6].

As the intermediary coat between the nickel-based superalloy and the TC, the BC enhances the bonding strength between the TC and the metal substrate. Moreover, it effectively inhibits the diffusion of external oxygen to the surface of the nickel-based superalloy, thereby preventing oxidation of the metal substrate in high-temperature environments [7]. The TC in the coating excels in providing heat insulation and corrosion protection. It not only lowers the surface temperature of the metal substrate through its unique microstructure but also effectively hinders the penetration of melt salt from the coating's surface to its interior in high-temperature environments, thereby offering exceptional protection of the metal substrate [8].

The TGO is a dense layer of thermal barrier coatings generated by the reaction of the BC with external oxygen in a high-temperature environment. The thin TGO effectively blocks external oxygen from infiltrating the bond layer, optimizing the coating's performance. However, if the thickness of TGO exceeds a specific threshold, the internal stress of the coating will be altered. This transformation shifts the internal compressive stress zone to a tensile stress area, resulting in cracks and delamination in the coating [9].

TBCs play a crucial role in enhancing the turbine engine's performance and service life [10]. The performance of the ceramic layer in TBCs directly influences their thermal shock resistance, mechanical properties and overall durability. Among the various ceramic materials used, Y_2O_3 partially stabilized ZrO_2 (YSZ) has emerged as the most widely adopted choice due to its advantageous properties [11]. YSZ exhibits low thermal conductivity, a thermal expansion coefficient that matches well with superalloys and exceptional fracture toughness, enabling the coating to perform optimally in demanding operating conditions [12]. However, the increasing thrust-to-weight ratio of engines has led to higher inlet temperatures, exceeding 1200 °C [13]. Under such extreme conditions, the t'-ZrO_2 phase present in the coating undergoes decomposition into t-ZrO_2 and c-ZrO_2. The martensitic transformation of t-ZrO_2 is triggered at this temperature [14]. Subsequently, the phase transformation induces a volumetric expansion of approximately 3–5%, accumulating significant stress within the coating. This stress accumulation adversely impacts the service life of the coatings [15].

To meet the stringent application demands of thermal barrier coatings in high-temperature environments, researchers have made significant progress in the development of various ceramic materials, such as rare earth zirconate, rare earth cerate, rare earth hexaaluminate and yttrium aluminium garnet [16–18]. However, these materials exhibit a low thermal expansion coefficient and poor fracture toughness. When the ceramic top coat of these materials is directly applied onto the bond coat, the thermal expansion mismatch stress accumulated in the coating under high-temperature conditions can result in cracks which reduces the coating's high-temperature service life [19]. To enhance the inadequate mechanical properties of the novel ceramic materials and further optimize their thermal insulation properties, researchers initiated the change of the material composition.

At the beginning of the 21st century, Ye *et al*. [20] first proposed the concept of high-entropy alloys. Compared with traditional alloys, high-entropy alloys exhibit high-entropy effects, slow diffusion effects, severe lattice distortion effects and "cocktail" effects, which have aroused researchers' interest in applying them to ceramic materials. In 2015, Rost *et al*. [21] prepared $(Mg_{0.2}Co_{0.2}Ni_{0.2}Zn_{0.2}Cu_{0.2})O$ high-entropy oxide ceramics for the first time, which exhibited excellent mechanical properties. With the continuous development of ceramic material synthesis and related technologies, research on high-entropy ceramics in the

field of thermal barrier coatings has been gradually increasing.

II. High-entropy ceramic composition design

High-entropy ceramics (HEC) is a single-phase ceramic system based on a multi-principal component high-entropy alloy design. In other words, the molar ratio of core elements in the system is designed according to equivalency (or near equivalency) without distinguishing between primary and secondary elements, similar to the design concept of decentralization [22]. As the number of principal elements in high-entropy ceramics increases, the number of material combinations increases exponentially, providing higher degrees of freedom for material optimization design. Taking the high-entropy ceramics of the $A_2B_2O_7$ system as an example, when there are five elements doped at both A and B sites, there will be 22.4 billion types of high-entropy ceramics [23]. Such a vast ceramics database will contain many options that cannot be prepared, used, or perform poorly. Therefore, researchers need to screen elements at different positions when designing ceramic components to reduce the complexity of material selection and improve design efficiency. To improve the design efficiency of high-entropy ceramic materials, researchers have proposed design criteria for high-entropy ceramics, mainly including atomic size criteria, lattice parameter criteria, and entropy criteria.

Entropy is a critical parameter in thermodynamics that can describe the degree of disorder in the internal lattice of high-entropy ceramics [24]. In the design of high-entropy materials, the size difference between different components is considered one of the important factors affecting material entropy [25]. By adjusting the difference in atomic size, the entropy value of the material can be effectively adjusted, thereby affecting the lattice structure and properties of the material. Therefore, the difference in atomic size between different components has become one of the criteria for high-entropy ceramics design [26]. The calculation formula for the average atomic size difference in high-entropy ceramic systems given by Nisar *et al*. [27] is as follows:

$$\delta = \sqrt{\sum_{i=1}^{N} X_i \left(1 - \frac{r_i}{\sum_{i=1}^{N} X_i \cdot r_i}\right)} \quad (1)$$

where X_i and r_i represent the molar content and atomic radius of the component i, respectively, and δ represents the atomic size mismatch parameter. Based on the Hume-Rothery rules and the atomic radius differences between different components in high-entropy alloys, researchers concluded that when $\delta \leq 6.6\%$, a single high-entropy ceramics can be obtained [28]. However, in the actual synthesis process of high-entropy ceramics, 6.6% is not an accurate size criterion for forming high-entropy ceramics. Glid *et al*. [29] prepared various boride ceramics based on size criteria and found that when the δ value was 3.5–8%, the prepared boride ceramics were a single solid solution. The numerical difference between the two criteria is related to the structure of high-entropy boride ceramics. Boride ceramics mostly have an AlB_2-type hexagonal structure, where B atoms form a layered structure similar to graphite, and metal atoms are interspersed between the layers. It is precisely due to the covalent solid characteristics of the B–B ring and M–B bond that there is no clear standard to effectively represent the actual bond length of different components. Jiang *et al*. [30] prepared 13 high-entropy perovskite ceramics with different rare earth elements compositions at different temperatures. According to Table 1, high-entropy perovskite ceramics could have been obtained when the δ value was 6–12%, and the atomic size mismatch parameter did not show a

Table 1. Summary of the key findings of all 13 compositions examined [30]

Composition	Secondary phase			δ	Tolerance factor
	1300 °C	1400 °C	1500 °C		
$Sr(Zr_{0.25}Sn_{0.25}Ti_{0.25}Hf_{0.25})O_3$	Minor	Minor	Major	6.7%	0.97
$Sr(Zr_{0.2}Sn_{0.2}Ti_{0.2}Hf_{0.2}Mn_{0.2})O_3$	Minor	Trace	No	11.2%	0.99
$Sr(Zr_{0.2}Sn_{0.2}Ti_{0.2}Hf_{0.2}Ce_{0.2})O_3$	Major	Major	Major	11.9%	0.95
$Sr(Zr_{0.2}Sn_{0.2}Ti_{0.2}Hf_{0.2}Y_{0.2})O_{3-x}$	Major	Minor	Trace	13.3%	0.95
$Sr(Zr_{0.2}Sn_{0.2}Ti_{0.2}Hf_{0.2}Ge_{0.2})O_3$	Trace	Trace	Major	11.2%	0.99
$Sr(Zr_{0.2}Sn_{0.2}Ti_{0.2}Hf_{0.2}Nb_{0.2})O_3$	Minor	Trace	No	6.0%	0.97
$Ba(Zr_{0.25}Sn_{0.25}Ti_{0.25}Hf_{0.25})O_3$	Minor	Minor	Major	6.7%	1.03
$Ba(Zr_{0.2}Sn_{0.2}Ti_{0.2}Hf_{0.2}Mn_{0.2})O_3$	Major	Major	Major	11.2%	1.05
$Ba(Zr_{0.2}Sn_{0.2}Ti_{0.2}Hf_{0.2}Ce_{0.2})O_3$	No	Minor	Major	11.9%	1.01
$Ba(Zr_{0.2}Sn_{0.2}Ti_{0.2}Hf_{0.2}Y_{0.2})O_{3-x}$	No	Major	Major	13.3%	1.01
$Ba(Zr_{0.2}Sn_{0.2}Ti_{0.2}Hf_{0.2}Ge_{0.2})O_3$	Minor	Minor	Major	11.2%	1.05
$Ba(Zr_{0.2}Sn_{0.2}Ti_{0.2}Hf_{0.2}Nb_{0.2})O_3$	No	Minor	Major	6.0%	1.03
$(Sr_{0.5}Ba_{0.5})(Zr_{0.2}Sn_{0.2}Ti_{0.2}Hf_{0.2}Nb_{0.2})O_3$	Minor	No	No	6.0%	1.00

significant correlation with the phase composition of high-entropy ceramics. This indicates that the role of the atomic size criterion in high-entropy ceramics composition design is limited. Therefore, researchers have begun to provide criteria for composition design from the perspective of crystal structure.

Since the atomic size criteria cannot provide sufficient theoretical support for the design of high-entropy ceramic components, researchers provide criteria for component design based on the lattice constants of each component. Gild *et al*. [29] proposed using lattice constants instead of atoms to calculate the size differences between components:

$$\delta_a = \sqrt{\sum_{i=1}^{N} X_i \left(1 - \frac{a_i}{\sum_{i=1}^{N} X_i \cdot a_i}\right)} \quad (2)$$

$$\delta_c = \sqrt{\sum_{i=1}^{N} X_i \left(1 - \frac{c_i}{\sum_{i=1}^{N} X_i \cdot c_i}\right)} \quad (3)$$

where a_i and c_i are the lattice parameters of the component i. By calculating and analysing δ_a and δ_c of the high-entropy metal diboride ceramics, it was concluded that δ_c can be regarded as a better criterion for forming high-entropy ceramic solid solutions. When $\delta_c \leq 6.2\%$, single-phase high-entropy ceramics can be effectively obtained, and the smaller the value of δ_c, the smaller the degree of lattice distortion, making it easier to prepare single-phase high-entropy ceramics. Based on the lattice parameter criteria, Chen *et al*. [31] found in the preparation of $(Y_{0.2}Yb_{0.2}Lu_{0.2}Eu_{0.2}Er_{0.2})_3Al_5O_{12}$ high-entropy yttrium aluminium garnet ceramics that single-phase high-entropy ceramic solid solutions could be obtained more efficiently when each component had the same crystal structure. This is because there is no need for a large amount of atomic rearrangement between different components during the solid-state reaction process. The required activation energy for the reaction is lower and the reaction rate is faster. This study provides sufficient theoretical support for designing high-entropy ceramics, making it easier for scholars to design high-entropy ceramics for thermal barrier coatings more efficiently.

In addition to the two high-entropy ceramics composition design criteria mentioned above, Sarker *et al*. [32] proposed using “entropy” as a criterion and referred to it as the entropy forming ability (EFA) for predicting and designing five-component metal carbide solid solutions:

$$EFA = \left(\sqrt{\frac{\sum_{i=1}^{n} g_i (H_i - H_{mix})^2}{\left(\sum_{i=1}^{n} g_i\right) - 1}}\right)^{-1} \quad (4)$$

where n is the total number of sampled geometrical configurations and g_i is the degeneracy. H_i is the enthalpy of formation at zero temperature of a supercell, and H_{mix} is the average of the enthalpies H_i of all of the possible supercell configurations. EFA is proportional to the width of energy distribution, and the higher the value, the easier it is to form single-phase high-entropy ceramics.

Saker *et al*. [32] screened five species from Ti, Zr, Hf, V, Nb, Ta, Mo and W to prepare high-entropy carbides and calculated the EFA values of 56 high-entropy carbides. By analysing XRD patterns, it was found that multi-phase formation is favoured in high-entropy carbide ceramics when EFA $\leq$ 45. Harrington *et al*. [33] prepared twelve high-entropy ceramics and analysed each ceramics' EFA and phase composition. The results showed that a second phase would form when EFA $\leq$ 45, and a single-phase high-entropy carbide would form when EFA $\geq$ 50. This result is consistent with Sarker's entropy criterion, providing sufficient theoretical support for the design of high-entropy ceramic components. However, in the actual design process, the entropy criterion also has certain limitations and its application scope is limited to five components high-entropy ceramics. It is hard to directly apply this criterion to predict the other components high-entropy ceramics.

Although the three criteria can provide specific theoretical references for the design of high-entropy ceramics, they all start from the synthesis of a single-phase high-entropy ceramic solid solution and assume that different components are mixed in equal proportions. However, there are still gaps in predicting the composition of non-equal-proportion high-entropy ceramics and predicting the performance of prepared ceramics. Therefore, improving the theoretical criteria for ceramics design is still an important research topic

III. Synthesis of high-entropy oxide powders

The synthesis of high-entropy ceramic materials is the basis for preparing new thermal barrier coating material. The distribution of different elements in ceramic materials, the particle size of powders, the flowability of powders, and the phase composition of powders directly affect their application in thermal barrier coatings [34]. Therefore, it is necessary to adopt the most suitable powder synthesis method based on different high-entropy ceramic powders and select the best preparation parameters to synthesize

ceramic materials with the best usage performance. The synthesis methods of ceramics mainly include the solid-state method and liquid-state method. The solid-state method refers to the contact and reaction of solid materials with different compositions in a high-temperature environment to obtain the required reaction products, often including the mechanical crushing method and solid-state reaction method [35]. The liquid-state method involves dissolving materials in the solution and changing different reaction conditions to enable different components to obtain target products through various reactions. These are mainly the sol-gel method, co-precipitation method and solution combustion method [36].

3.1. Solid-state reaction

The solid-state reaction method is the most widely used high-entropy ceramics synthesis method. It has the advantages of a simple preparation process, low cost, and large yield [37]. The specific steps are as follows: i) mix the dried oxides of different metals in proportion through ball milling, ii) grind the mixed powder and iii) prepare in a high-temperature environment to synthesize ultrafine powder of high-entropy ceramics [38]. The solid-state reaction process of high-entropy ceramics is mainly related to three factors [39–41]. The first is the contact area between different metal oxide powders. According to the calculation formula for specific surface area, the smaller the particle size of the metal powder, the larger the specific surface area, and the higher reaction activity can be exhibited. Obtaining high-entropy ceramics is more straightforward during the calcination process where reaction of different metal oxides occurs. Therefore, the metal oxides must be uniformly mixed and thoroughly ground before the solid-state reaction. Secondly, the structural differences between different metal oxides can affect the nucleation rate of high-entropy ceramics. When metal oxides have the same structure, the required reaction activation energy for solid-state reaction is lower, allowing for faster synthesis of ceramic materials. Conversely, if different metal oxides have different structures, the reaction becomes more complex, the synthesis temperature is higher and the reaction time is longer. The third factor is the ion diffusion rate, which is influenced by the crystal structure of metal oxides and the calcination temperature. The higher ion diffusion rate in high-temperature environment can effectively control the phase composition of the products.

Zhan *et al.* [42] used high-purity (>99.9%) powders of $SrCO_3$, ZrO_2, HfO_2, CeO_2, Yb_2O_3 and Gd_2O_3 as raw materials that underwent a solid-state reaction at 1400 °C for 24 h. Finally, $Sr(Zr_{0.2}Hf_{0.2}Ce_{0.2}Yb_{0.2}Me_{0.2})O_{3-x}$ (Me = Y, Gd) high-entropy ceramics containing a small amount of the second phase were prepared. Zhang *et al.* [43] prepared $(La_{0.2}Gd_{0.2}Y_{0.2}Yb_{0.2}Er_{0.2})_2(Zr_{1-x}Ti_x)_2O_7$ high-entropy ceramics with different Ti contents using La_2O_3, Gd_2O_3, Y_2O_3, Yb_2O_3, Er_2O_3, ZrO_2 and TiO_2 as raw materials and sintering at 1550 °C for 6 h. Chen *et al.* [31] prepared $(Y_{0.2}Yb_{0.2}Lu_{0.2}Eu_{0.2}Er_{0.2})_3Al_5O_{12}$ high-entropy ceramics by solid-state reaction method and analysed the phase compositions of the reaction products at three calcination temperatures of 1500, 1550 and 1600 °C. The XRD patterns of the reaction products at three environments are shown in Fig. 2 and it could be found that the reaction products consisted of a single yttrium-aluminium garnet structure only when the calcination temperature was 1600 °C. In contrast, diffraction peaks of $(Y_{0.2}Yb_{0.2}Lu_{0.2}Eu_{0.2}Er_{0.2})AlO_3$ and Al_2O_3 appeared in the XRD patterns of the reaction products at 1500 and 1550 °C, indicating that the calcination temperature had a significant effect on the physical phase composition of the reaction products. Although increasing the calcination temperature is conducive to a faster solid-phase reaction rate and promotes the synthesis of high-entropy ceramics with a single physical phase, high calcination temperatures increase the particle size of the prepared powders, which affects the flowability of the pelletized spherical powders during the thermal spraying process. To synthesize high-entropy ceramic powders with smaller particle sizes, researchers have begun to explore other powder synthesis methods.

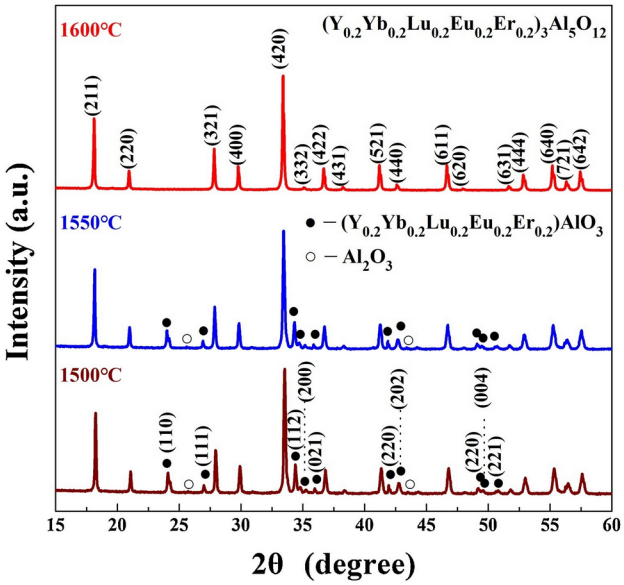

Figure 2. XRD patterns of samples calcined at 1500, 1550 and 1600 °C [31]

3.2. Sol-gel method

In the 1980s, the application of the sol-gel method in functional ceramics and composites gradually increased. At present, the widely used sol-gel method uses citrate ion as a complexing agent, generating

viscous gel through ethylene glycol and citric acid's esterification reaction to obtain nanometre-level powder particles [44].. In addition, citric acid can be used as a combustion agent, effectively reducing the temperature required for powder synthesis. Synthesis of the high-entropy ceramic powder by the sol-gel method consists of a few steps. First, dissolution of the proportionally mixed rare earth oxides into nitric acid to obtain a mixed solution of rare earth nitrates. This is followed by continuously stirring and mixing of metal nitrates, citric acid and ethylene glycol under the condition of water bath heating. Further on, the obtained gel is heated and dried, and finally ground and calcined to obtain powder particles [45]. The particle size of the powder obtained by the sol-gel method can reach the nanometre size, which is much smaller than that obtained by the solid-state reaction method.

$(La_{0.2}Y_{0.2}Nd_{0.2}Gd_{0.2}Sr_{0.2})CrO_3$ (LYNGSCO) high-entropy powder with a single perovskite structure was prepared by sol-gel method using $La(NO_3)_3{\cdot}6H_2O$, $Y(NO_3)_3{\cdot}6H_2O$, $Nd(NO_3)_3{\cdot}6H_2O$, $Gd(NO_3)_3{\cdot}6H_2O$, $Cr(NO_3)_3{\cdot}9H_2O$, $C_6H_8O_7{\cdot}H_2O$ and $HOCH_2CH_2OH$ as raw materials [46]. The powder morphology is shown in Fig. 3. The prepared powder exhibited slight agglomeration, which was consistent with uniformly distributed particles with a mean grain size of approximately 800–1000 nm and D_{50} = 938.7 nm.

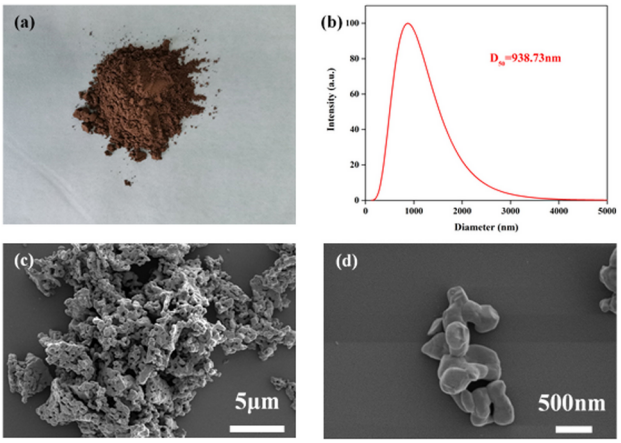

Figure 3. Photograph (a), particle size distribution curve (b) and microstructure (c,d) of LYNGSCO powder [46]

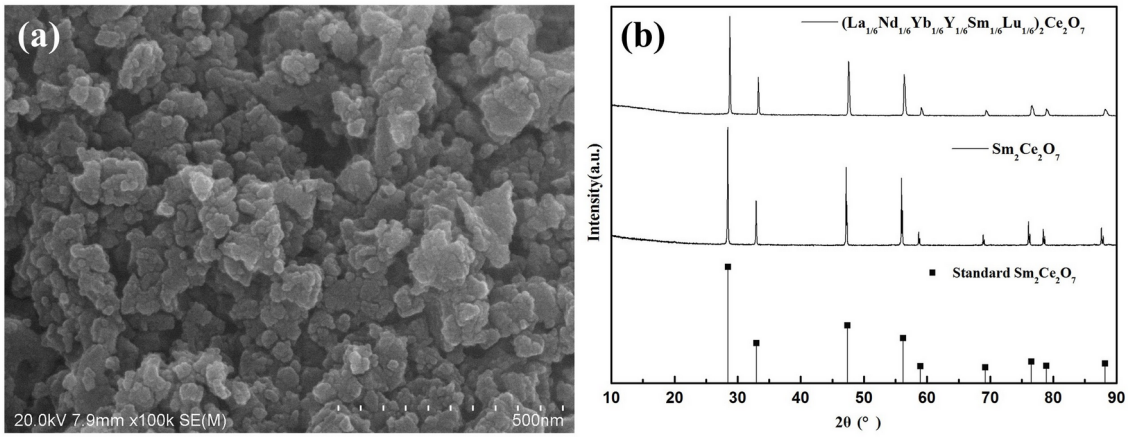

Figure 4. SEM image (a) and XRD pattern (b) of high-entropy oxide $(La_{1/6}Nd_{1/6}Yb_{1/6}Y_{1/6}Sm_{1/6}Lu_{1/6})_2Ce_2O_7$ powder [47]

Figure 4a shows the morphology of $(La_{1/6}Nd_{1/6}Yb_{1/6}Y_{1/6}Sm_{1/6}Lu_{1/6})_2Ce_2O_7$ high-entropy ceramic powder prepared by Zhang *et al*. [47] via sol-gel method, with an average particle size of 30–100 nm. In addition, the sol-gel method could give high-entropy ceramic powder with a single phase at a lower temperature environment, which was 300–400 °C lower than the synthesis temperature of the solid-state reaction method. Figure 4b shows the XRD patterns of prepared $(La_{1/6}Nd_{1/6}Yb_{1/6}Y_{1/6}Sm_{1/6}Lu_{1/6})_2Ce_2O_7$ high-entropy ceramic powder and $Sm_2Ce_2O_7$, which had almost the same diffraction peaks, indicating that powders with a single fluorite structure could be obtained by the sol-gel method. Although nanoscale powder particles can be obtained by the sol-gel method, which provides a specific technical basis for the development of nanoceramic materials and cold-sprayed nanostructured thermal barrier coatings, the complexity of the process of preparing ceramic powders using this method, the low productivity, the high cost of raw materials, and the environmental pollution caused by the evaporation of organic solvents in the process of milling and calcining, make it difficult for this method to be directly applied to commercial mass production.

3.3. Co-precipitation method

The co-precipitation method changes the equilibrium concentration of ions through the interaction between the precipitant and the metal salt solution so that each component can precipitate in a predetermined proportion in the container, thereby obtaining a uniform precipitate [48]. The co-precipitation method can offer uniform multi-component ceramic powder through high-speed

stirring, addition of a large amount of precipitant and by adjusting the acidity/alkalinity.

The co-precipitation method consists of a few steps. First, the salts of each of the corresponding components are mixed in the distilled water according to the predetermined proportion and stirred until a clear solution is formed. Second, a precipitant is added to the mixed solution to obtain a gel-like precipitate. Finally, the precipitate is calcined to obtain high-entropy ceramic powder [49]. Compared with the sol-gel method, the co-precipitation method obtains the ceramic powder with a single-phase composition through the reaction in the solution, which avoids the environmental risks caused by organic substances during the calcination process. In addition, the co-precipitation method can more easily obtain nanosize ceramic powder. The process flow of the co-precipitation method is more convenient and the preparation conditions are more straightforward, making it suitable for commercial mass production.

$(La_{0.2}Ce_{0.2}Nd_{0.2}Sm_{0.2}Eu_{0.2})_2Zr_2O_7$ powders with a single pyrochlore structure was prepared by co-precipitation method using $ZrOCl_2{\cdot}8H_2O$ and $LnNO_3{\cdot}6H_2O$ (Ln = La, Ce, Nd, Sm and Eu) [50]. In addition, $(La_{0.2}Ce_{0.2}Nd_{0.2}Sm_{0.2}Eu_{0.2})PO_4$ high-entropy ceramic powder with a single monazite structure was synthesized by co-precipitation using $RE(NO_3)_3{\cdot}6H_2O$ (RE = La, Ce, Nd, Sm and Eu) and H_3PO_4 as raw materials [51]. Although the co-precipitation method allows for more efficient synthesis of ceramic powders, the precipitant is not directly distributed throughout the solution by stirring. A localized area of high concentration will be formed at the location of contact between the precipitant and the solution, forming an inhomogeneous powder precipitation, leading to a deviation from the present ratio of rare earth elements within some of the ceramic powders which decreases the uniformity of the ceramics' properties.

3.4. Solution combustion method

The solution combustion method was developed in the mid-1980s as a new method to synthesize nanoscale ceramic powders [52]. The research on the low-temperature thermal decomposition of metal-hydrated hydrazine forms can be considered as the first application of this method. In this method, soluble metal nitrates were used as oxidants and organic fuels served as reducing agents [53]. The process involves ignition of the solution at a specific temperature and the heat required for combustion is provided through the solution's oxidation-reduction reaction to produce a fluffy ceramic powder. The solution combustion method was previously used to prepare metal oxide powders, and the preparation of nanoscale inorganic non-metallic powders was only developed in the later stage [54]. The solution combustion method is generally classified according to the different fuels, oxidants and solvents. Typical oxidants often include metal nitrates, while fuel choices are relatively broad, including urea, glycine, citric acid and acetylacetone [55]. The role of fuel is not only to provide sufficient heat to the system but also to ensure the formation of stable complexes with metal ions to increase their solubility and prevent selective precipitation of metal ions during dehydration [56]. Compared with other powder preparation methods, the solution combustion method has the advantages of a short preparation cycle, simple operation process, high purity of reaction products and low environmental pollution. Moreover, the prepared ceramic powder has uniform elemental composition and properties and broad application prospects in high-entropy ceramic powder preparation.

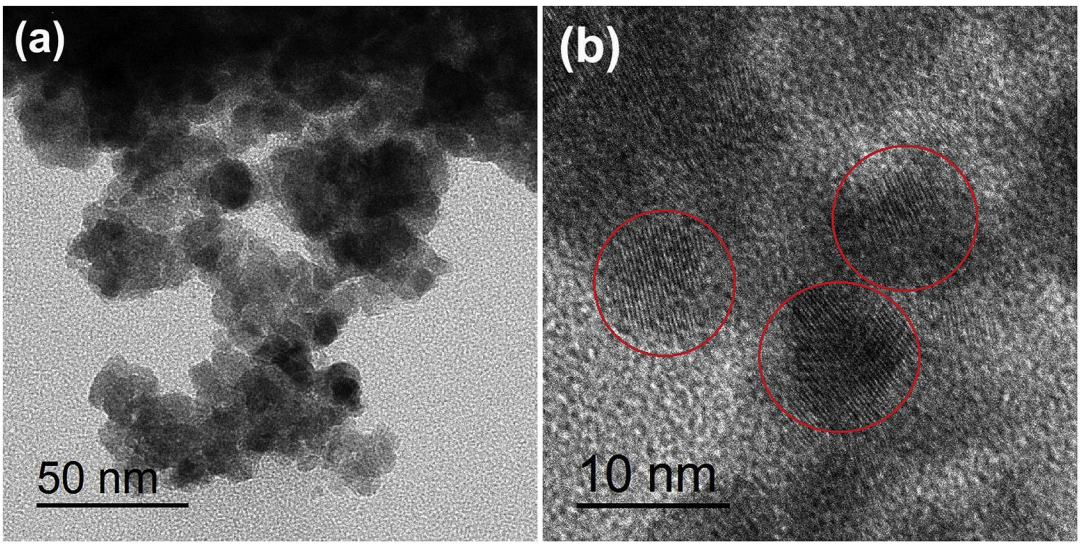

Figure 5. TEM images of the combustion prepared $(La_{0.2}Nd_{0.2}Sm_{0.2}Gd_{0.2}Yb_{0.2})_2Zr_2O_7$ high-entropy nanopowder [57]

Zhang *et al*. [57] prepared high-entropy $(La_{0.2}Nd_{0.2}Sm_{0.2}Gd_{0.2}Yb_{0.2})_2Zr_2O_7$ ceramic nanopowders by solution combustion method using $La(NO_3)_3{\cdot}6H_2O$, $Nd(NO_3)_3{\cdot}6H_2O$, $Sm(NO_3)_3{\cdot}6H_2O$, $Gd(NO_3)_3{\cdot}6H_2O$, $Yb(NO_3)_3{\cdot}6H_2O$ and $Zr(NO_3)_4{\cdot}5H_2O$ as raw materials. The glycine with purity ≥99 wt.% was introduced as the incendiary agent. The powder morphology is shown in Fig. 5. The particle size of the prepared powder was 8–10 nm, which was much lower than that of the solution combustion synthesized powders of other $A_2B_2O_7$ systems.

IV Fabrication of TBC with high-entropy oxides

Conventional thermal barrier coatings are manufactured mostly by using electron beam physical vapour deposition (EB-PVD), atmospheric plasma spraying (APS) and electrophoretic deposition (EPD), but some other deposition techniques which can use previously synthesized powders are also developed.

Although with liquid-state methods someone can obtain high-entropy ceramic powders with single phase, uniform element distribution and small particle size, these powders cannot directly participate in the thermal spraying process. This is because nanoscale powders have poor flowability. During the plasma spraying process, the powder will adhere to the inner surface of the powder delivery pipeline, reducing the deposition efficiency of the powder. Moreover, it is challenging for smaller ceramic powders make to enter the centre of the plasma flame flow. Therefore, further thermal treatment of the powder is needed to increase the particle size of the ceramic powder.

In recent years, high-entropy ceramic materials have emerged as promising candidates for thermal barrier coating applications due to their excellent performance. However, there are only a few reports on high-entropy thermal barrier coatings, and existing research primarily focuses on their preparation using atmospheric plasma spraying and laser cladding techniques.

Atmospheric plasma spraying has the characteristics of high deposition efficiency, simple equipment operation, and low cost [58]. The powder velocity is high during the spraying process, providing excellent bonding strength between the molten powder and the metal substrate [59]. As a traditional coating preparation method, it is widely used to prepare high-entropy thermal barrier coatings. Xue *et al*. [60] prepared gradient high-entropy $(La_{0.2}Nd_{0.2}Sm_{0.2}Eu_{0.2}Gd_{0.2})_2Ce_2O_7$/YSZ thermal barrier coatings by APS and compared the thermal shock behaviour with double-layer coatings. The results showed that the double-layer structure coating formed a through crack after 12 thermal shock cycles. In comparison, the gradient structure thermal barrier coating only showed partial peeling on the surface after 48 thermal shock cycles, indicating that gradient design is beneficial for alleviating thermal stress inside the coating. Ma *et al*. [61] investigated the effect of spray power on the thermal conductivity of high-entropy $(La_{0.2}Sm_{0.2}Eu_{0.2}Yb_{0.2}Y_{0.2})_2(Ce_{0.5}Zr_{0.5})_2O_7$ coatings. The results showed that lower spray power was beneficial for increasing the concentration of oxygen vacancies in the coatings and reducing the thermal conductivity.

Laser cladding, a multidisciplinary technology combining laser and computer-aided control technology, was also used for preparation of high-entropy coating [62]. Laser cladding is a surface treatment method that uses a high-energy density laser beam as a heat source to simultaneously melt the substrate and cladding material and prepare a coating [63]. Compared with atmospheric plasma spraying, laser cladding technology has the following advantages: i) after laser cladding, the coating material forms a metallurgical bond with the substrate and exhibits excellent bonding performance, ii) the coating preparation time is short, the cooling rate is fast and it is easy to form small microstructures and improve work efficiency and iii) the coating composition can be controlled, the operation is simple and it is easy to achieve automated production [64]. Therefore, laser cladding technology is considered as a high-entropy thermal barrier coating preparation technology with good application prospects. In one study, Zhang *et al*. [65] prepared $La_2(Ti_{0.2}Zr_{0.2}Sn_{0.2}Ce_{0.2}Hf_{0.2})_2O_7$ high-entropy coating on the YSZ surface by laser cladding and characterized the thermal cycling life of the coating. The results indicate that due to the effective alleviation of thermal stress inside the coating by the double-layer structure, the thermal shock life of the laser cladding coating can reach 60 times.

V. Sintering of high-entropy ceramics

Synthesis of ceramic powders is only the first step in sample fabrication and usually it is necessary to apply sintering to produce final desirable product. Ceramics sintering usually refers to placing stacked ceramic powders in a high-temperature environment under specific temperature and atmosphere conditions. Powder materials achieve atomic diffusion under high temperatures, gradually reducing the gap between particles inside the powder. This eliminates moisture, binders, pores, etc. in the ceramic green body, resulting in volume shrinkage and densification of the ceramic powder. At present, the advanced sintering methods for high-entropy ceramics mainly include common sintering, ultra-fast high-temperature sintering, spark plasma sintering and flash sintering.

5.1. Common sintering

Common sintering (CS) is a sintering method in which a press-formed ceramic green body is placed into a conventionally heated furnace and conventional heating is utilized to complete the densification process of the sample at high temperatures [66]. Common sintering is the most frequently used and mature method for preparing and producing ceramics due to its low consumables and simple equipment. The common sintering process requires both a driving force and a material transfer process so that the pores in the green body gradually diffuse, shrink and disappear, increasing the density of the green body [67].

At present, researchers study the material transfer mode and mechanism in the sintering process of ceramics, mainly including the evaporation-condensation material transfer mechanism and material transfer by diffusion. In the high-temperature process, due to the different surface curvature of the powder particles, there are different vapour pressures in different parts of the system. There is a tendency of mass transfer through the gas phase and this mass transfer process is only carried out at the high temperature of the system with higher vapour pressure [68]. Due to the relatively low vapour pressure of many ceramic materials at high ambient temperatures, evaporation-condensation material transfer is difficult. Therefore, the material transfer is carried out by diffusion mass transfer. During the initial stage of sintering, the combined impact of hydrostatic pressure and localized shear stress causes the particles to rearrange, resulting in a notable reduction in the porosity and shrinkage of the ceramic green body [69].

Li *et al*. [70] used common sintering to prepare six high-entropy oxide ceramics such as $(La_{0.2}Nd_{0.2}Sm_{0.2}Eu_{0.2}Gd_{0.2})_2Zr_2O_7$ with pyrochlore structure by using seven oxides, namely, ZrO_2, La_2O_3, Nd_2O_3, Sm_2O_3, Eu_2O_3, Gd_2O_3 and Y_2O_3 as raw materials. It was found that a single-phase pyrochlore structure was obtained when temperature was increased to 1000 °C (Fig. 6). In addition, as the sintering temperature increased to 1500 °C, the half peak width of the (400) diffraction peak decreased and the crystallinity of the sample was increased.

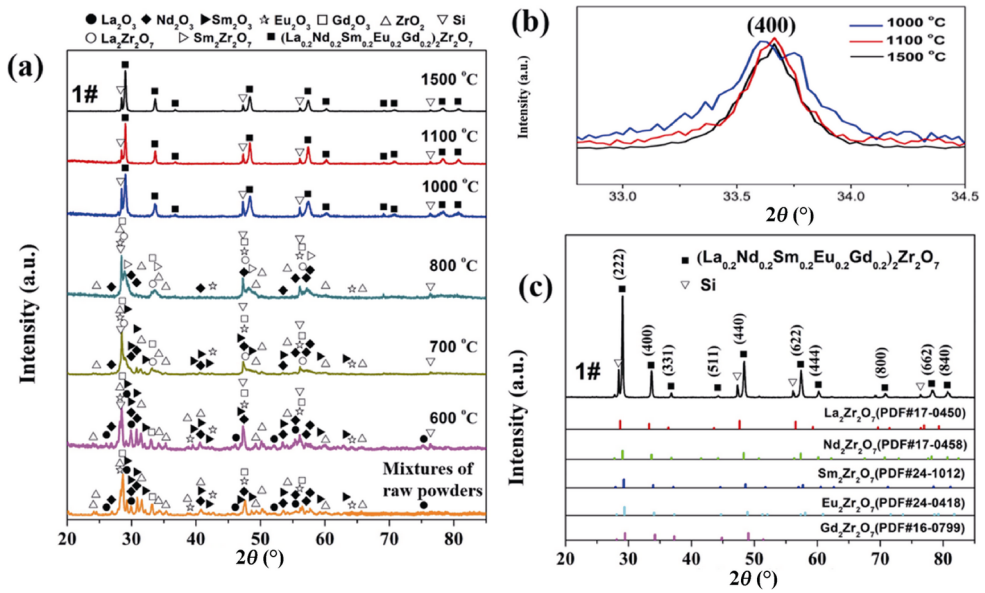

Figure 6. XRD patterns of the mixtures of raw powders and ceramic products (a) and corresponding zoom-in view of (400) diffraction peaks. XRD pattern of ceramics sintered at 1500 °C for 3 h (c) [70]

5.2. Ultra-fast high-temperature sintering

Traditional high-entropy ceramics sintering densifies ceramics by providing the energy required during the sintering process through external heating under no-pressure conditions. Due to the simple equipment, convenient manual operation and large ceramics size used in traditional sintering methods, this sintering technology is still widely used. However, traditional ceramics sintering processes typically have a slow heating rate (generally below 20 °C/min), resulting in the prolonged sintering heating and holding times [71]. This is especially true for ceramics with high melting points or complex crystal structures, where the entire sintering cycle can last up to several tens of hours. Such low production efficiency limits the preparation and application of ceramic materials and the long-term heating process causes serious energy waste. Therefore, researchers have been committed to exploring new ceramics sintering technologies to improve the sintering efficiency of ceramics while shortening the sintering time to obtain small grain size ceramics with better performance.

In 2020, Wang *et al*. [72] first proposed the ultra-fast high-performance sintering technology and used it

to achieve the sintering of $Li_{1.3}Al_{0.3}Ti_{1.7}(PO_4)_3$ ceramics. This method improves ceramic components' screening efficiency by optimizing the ceramics sintering process. The ultra-fast high-performance sintering technology can complete the densification process of ceramics in 10 s, significantly reducing the preparation cycle of ceramics. The working principle of ultra-fast sintering technology is shown in Fig. 7 [73]. Firstly, the precursor powder of the target product is pressed and formed on a press and then placed inside the graphite felt. Secondly, graphite felt generates a large amount of Joule heat under the action of electric current, which quickly reaches a high temperature (up to 3000 °C) in the entire sintering system. Finally, the precursor powder coated with graphite inside the carbon felt reaches a high sintering temperature in a very short time, thereby achieving densification within an ultra-short sintering cycle.

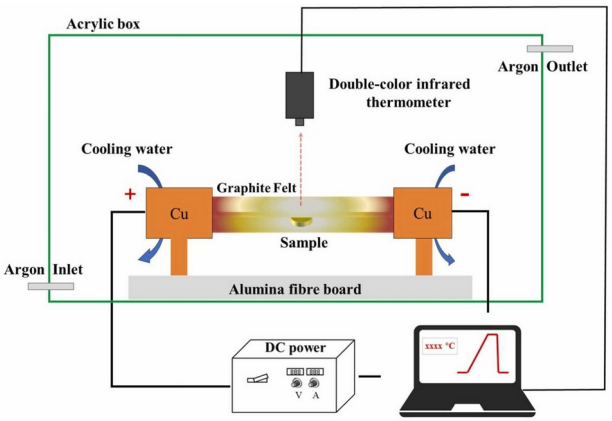

Figure 7. Schematic of the UHS system [73]

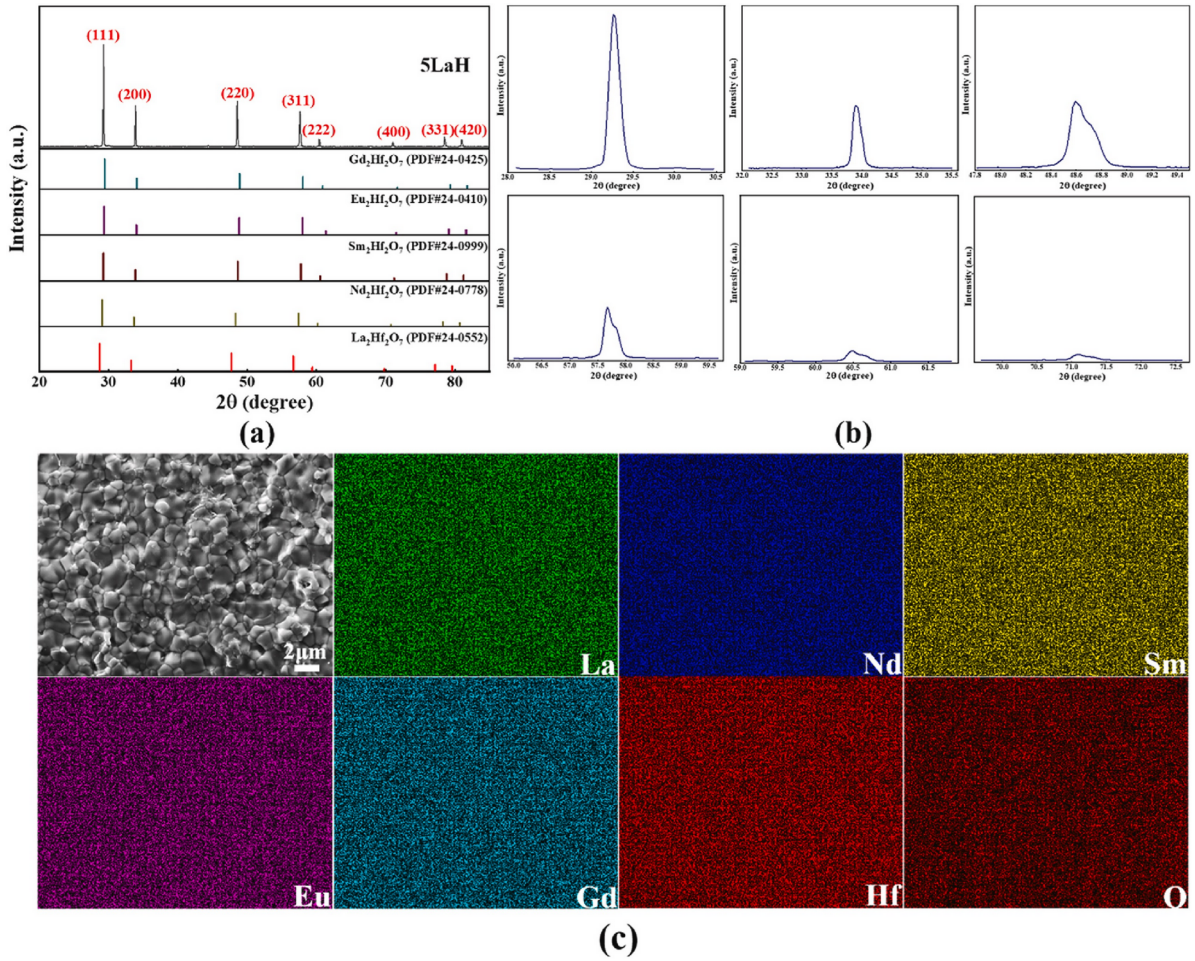

Figure 8. XRD pattern of the 5LaH (a), the enlarged view of the six prominent peaks (b) and the microstructure and element distribution of the 5LaH (c) [74]

At present, ultrafast high-speed sintering technology has been applied to the high-entropy ceramic materials for thermal barrier coatings. Ye *et al*. [74] prepared $(La_{0.2}Nd_{0.2}Sm_{0.2}Eu_{0.2}Gd_{0.2})_2Hf_2O_7$ (5LaH) high-entropy ceramics by ultra-fast high-temperature sintering and characterized their structures. The results are shown in Fig. 8. The sintered high-entropy ceramics had a single fluorite structure and the elements were uniformly distributed in the ceramic blocks without elemental bias. In addition, Ye *et al*. [75] used this method to prepare defective fluorite-phase high-entropy $(Y_{0.2}Dy_{0.2}Er_{0.2}Tm_{0.2}Yb_{0.2})_4Hf_3O_{12}$. The sintering process involved a stepwise temperature increase and the

samples were sintered at a current of 52 A for 150 s. The high-entropy oxide ceramics had a high thermal expansion coefficient (11.23×10^{-6} K^{-1}) and very low thermal conductivity (0.94 $W\cdot m^{-1}\cdot K^{-1}$ at 1300 °C). The average grain sizes of the samples obtained by ultra-fast high-temperature sintering were 1.20, 1.68 and 2.08 μm after annealing at 1500 °C for 10, 15 and 20 h, respectively. The growth of the grains was extremely slow, attributed to the non-equilibrium property of ultra-fast high-temperature sintering and the high-entropy material's non-equilibrium features.

Since 2020, ultra-fast high-temperature sintering has attracted the attention of researchers since it has a few advantages [75–78]. Firstly, it is simple and has easy-to-operate sintering equipment, i.e. ultra-fast high-temperature sintering utilizes electrified graphite felt for heating [75]. Hence, the construction of sintering equipment is relatively simple, requiring only a programmable DC power supply with stable output. Secondly, high heating rate and sintering temperature can be obtained. The heating rate of ultra-fast high-temperature sintering can be present through a programmable power supply, thus enabling precise control of the temperature of graphite felt. Moreover, due to the high melting point of carbon, as long as the current is large enough, graphite felt can heat the sample to 3000 °C, which theoretically can densify the vast majority of ceramics. Finally, sintering ceramics with complex shapes can be prepared The sample's complex shape is almost not damaged after sintering because it is wrapped inside the graphite felt during ultra-fast high-temperature sintering.

5.3. Spark plasma sintering

Spark plasma sintering (SPS) is a new type of rapid sintering technology that has been developed in recent years. This technology involves directly applying pulsed current between powder particles for heating and sintering [79]. Hence, it is also known as plasma-activated sintering or plasma-assisted sintering. This technology applies the on/off DC pulse voltage generated by a particular power control device to the powder [80,81]. On the one hand, it can use the usual discharge to promote sintering. Pulse discharge can cause spark discharge between powders, achieving densification through an instantaneous high-temperature field. Figure 9 is a schematic diagram of spark plasma sintering [82]. Due to the strong pulse current applied between powder particles, spark plasma sintering can generate many effects conducive to rapid sintering. Compared with traditional sintering methods, spark plasma sintering has the advantages of a fast-heating rate, short sintering time, low sintering temperature, uniform grain size, favourable control of the fine structure of the sintered body and high material density [83,84].

The explanation of the mechanism of spark plasma sintering mainly includes two types. The first explanation suggests that during the sintering process, powder particles form positive and negative electrodes under the induction of an electric field. Under the action of pulsed current, discharge phenomena occur between particles of different electrodes, and plasma is excited. When the plasma generated by discharge collides with the contact positions between ceramic particles, it causes evaporation on the surface of ceramic particles and increases the activation degree of the powder contact positions. At this point, the electrical energy stored in the dielectric layer of the particle cluster begins to be released, and the dielectric layer undergoes intermittent rapid discharge. The self-heating generated by the final rapid discharge will complete the sintering of ceramic powder [85]. The second explanation suggests that the instantaneous on/off of a DC pulse circuit will form a discharge plasma during the sintering process, activating the surface of ceramic particles and generating internal heat. Finally, the ceramic powder is sintered under the combined action of internal heat and discharge shock pressure [86].

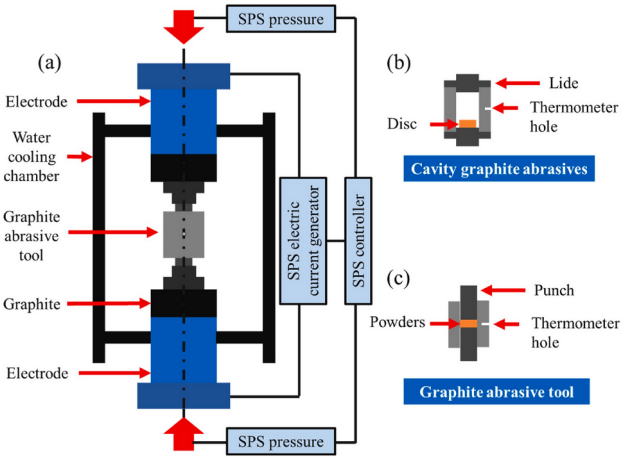

Figure 9. Schematic presentation of the SPS process and two different kinds of graphite abrasive tools [82]

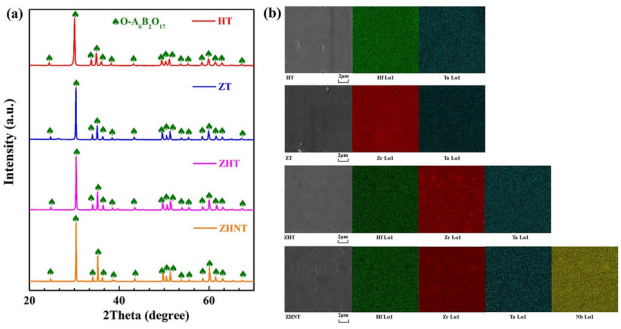

Figure 10. XRD patterns (a) and SEM images and corresponding EDS mapping (b) of the as-sintered bulk $A_6B_2O_{17}$ ceramics [87]

At present, spark plasma sintering has been applied for the sintering of high-entropy ceramics. Tan *et al*. [87] prepared four $A_6B_2O_{17}$-type ceramic green bodies using SPS, which included $Hf_6Ta_2O_{17}$ (HT), $Zr_6Ta_2O_{17}$ (ZT), $(Zr_{2/3}Hf_{1/3})_6Ta_2O_{17}$ (ZHT) and $(Zr_{2/3}Hf_{1/3})_6(TaNb)_2O_{17}$ (ZHNT). Figure 10 illustrates the four ceramics' surface morphologies and elemental distributions after sintering. The average grain sizes of the HT, ZT, ZHT, and ZHNT ceramics were 1.1±0.8, 0.96±0.5, 1.3±0.7 and 1.74±0.9 μm, respectively. Additionally, Hf, Zr, Ta and Nb were uniformly distributed in all ceramics and no secondary phase was detected.

$(La_{1/7}Nd_{1/7}Sm_{1/7}Eu_{1/7}Gd_{1/7}Dy_{1/7}Ho_{1/7})_2Zr_2O_7$ high-entropy ceramics and $Gd_2Zr_2O_7$ (GZO) ceramics were prepared by reactive spark plasma sintering (RSPS) and the morphology and elemental distribution of the two ceramics were compared after sintering (Fig. 11) [88]. All elements were uniformly distributed inside the ceramics. Due to the synergistic effect of compositional complexity and severe lattice distortion, the grain size of $7RE_2Zr_2O_7$ ceramics was only 1.45 μm, about 1/6 of the average grain size of GZO.

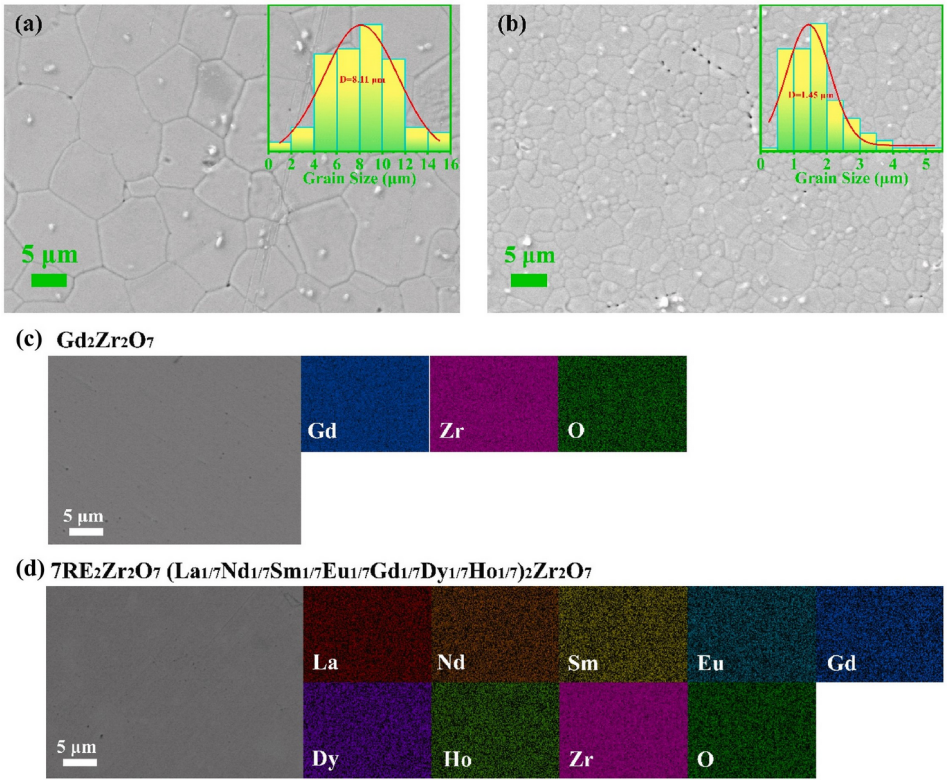

Figure 11. SEM images and statistical diagrams of the average grain size of $Gd_2Zr_2O_7$ (a) and $7RE_2Zr_2O_7$ (b). SEM images and corresponding EDS mapping of polished surfaces of $Gd_2Zr_2O_7$ (c) and $7RE_2Zr_2O_7$ (d) [88]

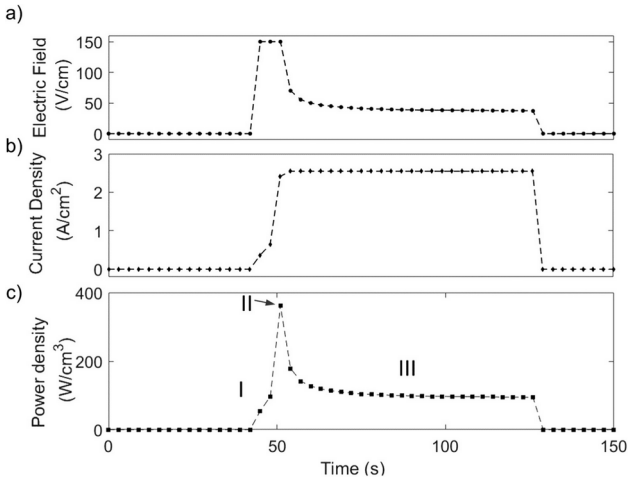

Figure 12. Sintering parameters against time in flash sintering experiment [90]

5.4. Flash sintering

Flash sintering (FS) belongs to the electric current-assisted sintering and has gained the attention of researchers due to the extremely short sintering time. The flash sintering technique was first reported in 2010 by Cologna *et al*. [89]. They subjected zirconia blanks to an electric field of 40 V/cm, causing rapid sample warming by the Joule heating effect and resulting in sample densification at the temperature of 850 °C within a few seconds. According to the changes in parameters such as current, voltage and power loss, flash sintering can be divided into three stages (Fig. 12) [90]. The first, latent stage, where the resistivity of the sample decreases as the temperature increases and the current through the sample increases gradually. In the second flash sintering stage, the resistivity and voltage of the sample plummet and the

current and power loss increase sharply. The third, stabilization stage, where the sample's current, voltage and power loss enter a steady state. The most apparent advantages of flash sintering over conventional sintering are the significant reduction in sintering time and temperature. The sintering time of flash sintering can be shortened to a few minutes or even seconds and the furnace temperature can be lowered by several hundred degrees or even down to 1000 °C, which effectively avoids the problems of coarse grain size caused by holding the sample at a high temperature for a long time.

$(La_{0.2}Nd_{0.2}Sm_{0.2}Eu_{0.2}Gd_{0.2})_2Zr_2O_7$ high-entropy pyrochlore ceramics was prepared by using reactive flash sintering at 1200 °C for 1 min, with an electric field strength of 9 V/mm and applied pressure of 10 MPa [91]. In addition, the authors explored the effects of different current densities on the relative density, hardness and Young's modulus of the sintered bodies, then compared them with the solid-state sintering samples sintered at 1600 °C for 3 h and 6 h. When the current density was increased from 60 to 200 mA/mm^2, the average grain size of the sintered body increased from 0.6 to 2.4 μm, and the relative density increased from 91% to 99%. The relative density of the solid-state sample sintered for 6 h was 97%, which was lower than that of the flash sintered sample at 200 mA/mm^2. The average grain size of the solid-state sintered sample was 5.2 μm, which was more significant increase than that of the flash sintering sample. In terms of mechanical properties, the $(La_{0.2}Nd_{0.2}Sm_{0.2}Eu_{0.2}Gd_{0.2})_2Zr_2O_7$ ceramics prepared by flash sintering had better hardness and fracture toughness than the solid-state sintered samples.

Zhao *et al*. [92] prepared high-entropy pyrochlore ceramics $(La_{0.2}Nd_{0.2}Sm_{0.2}Eu_{0.2}Gd_{0.2})_2Zr_2O_7$ using reactive flash sintering. They systematically investigated the phase transformation process, densification process and grain growth of high-entropy ceramics during the flash-firing process. The analysis revealed that the sample initially contained a mix of pure oxides and a small amount of high-entropy phase during the first 10 s before the flash sintering began. After 1 s of the flash sintering, most of the sample had transformed into the high-entropy phase, although some peaks of the pure oxides were still present. After 5 s of flash sintering, all the pure oxides had changed into $(La_{0.2}Nd_{0.2}Sm_{0.2}Eu_{0.2}Gd_{0.2})_2Zr_2O_7$. When the flash sintering time was extended to 180 s, the sample's crystallinity increased, and the diffraction peaks of the high-entropy pyrochlore became more distinct.

VI. Properties of high-entropy ceramics

In recent years, the performance of high-entropy ceramics for thermal barrier coatings has been the focus of research, including thermodynamic properties, thermal insulation, corrosion resistance, high-temperature phase stability and chemical compatibility. Due to the high-entropy effect, high-entropy ceramics have different properties from single-component ceramics, enabling them to adapt to more complex environments.

6.1. Thermal conductivity

Thermal conductivity is one of the most critical performance parameters of thermal barrier coatings, reflecting their insulating effect in high-temperature environments. The lower the thermal conductivity, the lower the surface temperature of the metal substrate and the higher the temperature of the front inlet of the turbine engine. Thus, this contributes to the improvement of the engine thrust-to-weight ratio and fuel efficiency [93]. There are two main strategies for insulating thermal barrier coatings. The first aims to prevent the conduction of external heat flow to the metal substrate by addressing the horizontal cracks within the coating. The second focuses on phonon scattering through micro-cracks, pores and defects within the ceramic material to reduce thermal conductivity by decreasing the phonon mean free path [94,95]. Since thermal barrier coatings operate mainly at ≥1100 °C, where heat transfer to the interior of the coating through phonon is favoured, only the impact of high-entropy ceramics on phonon scattering is discussed. The equations for the thermal conductivity of phonons are as follows [96]:

$$k = \frac{1}{3}\frac{C_v}{\nu} \tag{5}$$

$$C_v = \left(\frac{\partial U}{\partial T}\right)_V \tag{6}$$

where k is the thermal conductivity of the phonon, C_v is the specific heat capacity of the phonon, v is the average velocity of the phonon, independent of the ambient temperature, l is the phonon mean free path, U is the energy and T is the temperature. The C_v can be simplified using the Dulong-Petit law when the ambient temperature of high-entropy ceramics exceeds the Debye temperature. In this case, the thermal conductivity of high-entropy ceramics can be determined by the mean free path of phonon, making it more manageable than calculating C_v directly through Eq. 6. The extent of phonon scattering can be determined using following equation [96]:

$$\frac{1}{l} = \frac{1}{l_c} + \frac{1}{l_b} + \frac{1}{l_i} \tag{7}$$

where l_c, l_b and l_i represent the complexity, grain boundaries and lattice distortion of high-entropy ceramic crystals, respectively. Since high-entropy ceramics are formed by mutual solid solutions of multiple metal oxides, there are numerous lattice

distortions inside the crystals. In addition, due to the significant ionic radius differences within the high-entropy ceramics and the large charge differences between cations and anions, there are sizeable chemical bond length differences as well as Coulomb force differences in the ceramics, leading to a more complex internal crystal structure, a significant increase in the degree of phonon scattering and a significant decrease in thermal conductivity [97].

Zhu *et al.* [98] prepared two high-entropy ceramics, $(La_{0.2}Nd_{0.2}Y_{0.2}Er_{0.2}Yb_{0.2})_2Zr_2O_7$ (LNYEYZO) and $(La_{0.2}Nd_{0.2}Sm_{0.2}Gd_{0.2}Yb_{0.2})_2Zr_2O_7$ (LNSGYZO), by the solid-state method and compared their thermal conductivities with $La_2Zr_2O_7$ and $Yb_2Zr_2O_7$ from 100 to 600 °C. The results showed that due to the significant lattice distortion inside the high-entropy ceramics and phonon scattering, the thermal conductivities of LNYEYZO and LNSGYZO were 1.62–1.59 and 1.74–1.75 $W \cdot m^{-1} \cdot K^{-1}$, respectively, i.e. much lower than the thermal conductivities of $La_2Zr_2O_7$ and $Yb_2Zr_2O_7$ in the same environment. Zhao *et al.* [99] prepared $(Y_{0.25}Yb_{0.25}Er_{0.25}Lu_{0.25})_2(Zr_{0.5}Hf_{0.5})_2O_7$ by solid-state method and analysed its thermal conductivity at room temperature environment, which showed that due to the lattice distortion caused by the solid solution of multiple components within each other, its thermal conductivity was only 1.40 $W \cdot m^{-1} \cdot K^{-1}$, which was much lower than the YSZ at room temperature.

Liu *et al.* [100] prepared single-phase $(Y_{0.2}Sm_{0.2}Eu_{0.2}Er_{0.2}Er_{0.2}Yb_{0.2})_2Si_2O_5$ high-entropy ceramics with single-component silicate ceramics and the results are presented in Fig. 13. The high concentration of oxygen vacancies inside the high-entropy ceramics, along with the disordered arrangement of cations, contributes to the ceramic materials' good infrared reflectance. Consequently, the thermal conductivity of the high-entropy ceramics was only 0.96±0.03 $W \cdot m^{-1} \cdot K^{-1}$.

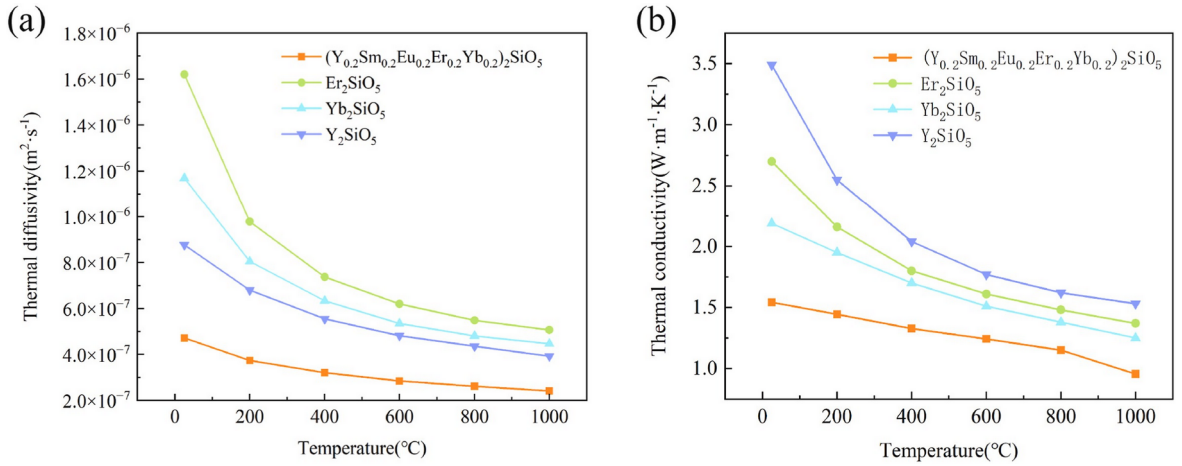

Figure 13. Thermal diffusivities and thermal conductivities of $(Y_{0.2}Sm_{0.2}Eu_{0.2}Er_{0.2}Yb_{0.2})_2SiO_5$ and several silicates with X_2-Re_2SiO_5 structure: a) thermal diffusivities and b) thermal conductivities [100]

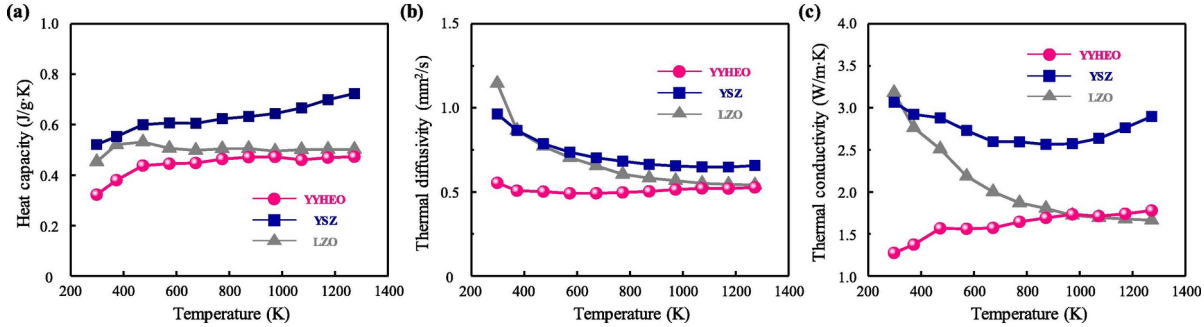

Figure 14. Thermal properties of YYHEO ceramics represented by: a) heat capacity, b) thermal diffusivity and c) thermal conductivity [101]

Song *et al.* [101] prepared single-phase $(Y_{1/2}Yb_{1/2})_2(Ti_{1/3}Zr_{1/3}Hf_{1/3})_2O_7$ (YYHEO) high-entropy ceramics by a solid-state reaction method and compared their thermal properties with YSZ and $La_2Zr_2O_7$ (Fig. 14). The thermal conductivity of YYHEO at 298 K was only 1.27 $W \cdot m^{-1} \cdot K^{-1}$, much lower than for YSZ and LZO. This low thermal conductivity was attributed to the unique defective fluorite structure of YYHEO, where the random distribution of cations and oxygen vacancies resulted in substantial lattice distortions and reduced the phonon's mean free path. Additionally, YYHEO processed vibration modes as diffusions that partially

localized without well-defined polarization, led to a glass-like thermal conductivity.

Low thermal conductivity mechanism of $(Gd_{0.25}Sm_{0.25}Yb_{0.25}Y_{0.25})_3TaO_7$ high-entropy ceramics was analysed by Sang *et al*. [102]. They found that Re^{3+} ions enter the lattice of Ta_2O_5 to form a substitutional solid solution. Based on the local electroneutrality principle of the lattice, oxygen vacancies were created when Re^{3+} replaces Ta^{5+} in the lattice (Eq. 8). These oxygen vacancies led to the increase of the phonon non-harmonic vibration, which in turn decreased the phonon mean free path and reduced the overall thermal conductivity of the ceramics.

$$RE_2O_3 \xrightarrow{Ta_2O_5} 2RE''_{Ta} + 3O_O^{\times} + 2V_O^{\cdot\cdot} \qquad (8)$$

6.2. Fracture toughness

Fracture toughness is one of ceramic materials' crucial mechanical properties for thermal barrier coatings. It measures the toughness of thermal barrier coatings and represents ceramic materials' ability to prevent crack expansion [103]. To ensure the thermal barrier coating's excellent service life in high-temperature environments, the ceramic material should possess the highest possible fracture toughness.

Phase transition toughening occurs primarily within the YSZ coating. When the stress near the crack tip is high, it causes the ZrO_2 to change from the tetragonal phase to the monoclinic phase, absorbing significant stress at the crack [104]. Due to the excellent high-temperature phase stability of pyrochlore, monazite and yttrium aluminium garnet ceramics used for thermal barrier coatings, it is difficult to perform phase transition toughening. Therefore, the primary toughening method for these materials is the ferroelastic domain transformation. Toughening by ferroelastic domain transformation is based on the lattice rearrangement that occurs in ceramic materials under stress, which produces plastic deformation and achieves toughening while consuming the stress in the region near the crack. Thus, the stress required for lattice rearrangement decreases as the ambient temperature of the ceramics rises, so that the ferroelastic domain transformation can play a better role in toughening in high-temperature environments [105]. Toughening via ferroelastic domain transformation is more accessible due to the large number of lattice distortions within high-entropy ceramics.

Zhu *et al*. [106] created high-entropy ceramics $(Dy_{0.2}Ho_{0.2}Er_{0.2}Y_{0.2}Yb_{0.2})_3NbO_7$ and compared their fracture toughness with single-component $RENbO_7$. The results showed that the high-entropy ceramics had a fracture toughness of 2.13 $MPa{\cdot}m^{1/2}$, much higher than that of the single-component $RENbO_7$ and YSZ, due to the grain refinement caused by doping with several rare earth elements. Luo *et al*. [107] prepared two high-entropy ceramics, $(La_{0.2}Nd_{0.2}Sm_{0.2}Eu_{0.2}Gd_{0.2})_2Zr_2O_7$ (LaHZ) and $(Yb_{0.2}Nd_{0.2}Sm_{0.2}Eu_{0.2}Gd_{0.2})_2Zr_2O_7$ (YbHZ), and compared their fracture toughness with $La_2Zr_2O_7$. The results showed that YbHZ exhibited the highest fracture toughness, indicating that addition of Yb^{3+} was beneficial for improving the formation and expansion mode of microcracks in high-entropy ceramics. This optimization of mechanical properties was achieved through the significant lattice distortion caused by the high-entropy effect.

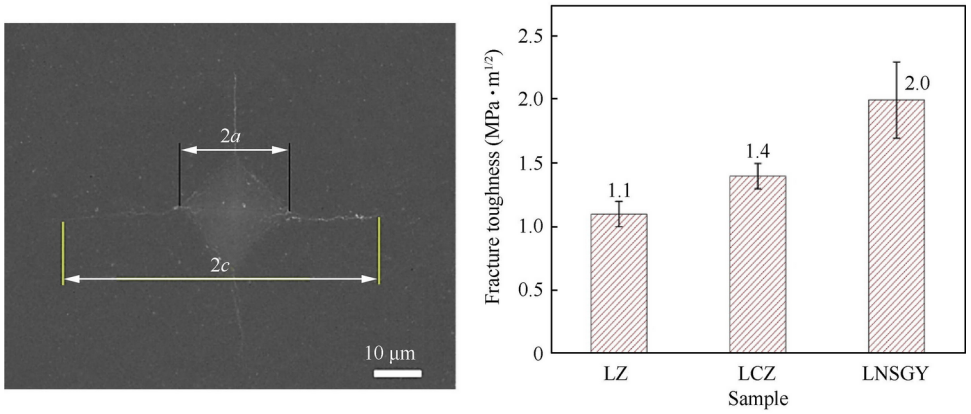

(a) Indentation photograph of LNSGY ceramic (b) Fracture toughness of LZ, LCZ and LNSGY ceramics

Figure 15. Indentation photograph of LNSGY ceramics and fracture toughness of LZ, LCZ and LNSGY ceramics [108]

Guo *et al*. [108] used solid-state reaction method to prepare $(La_{0.2}Nd_{0.2}Sm_{0.2}Gd_{0.2}Yb_{0.2})_2(Zr_{0.75}Ce_{0.25})_2O_7$ (LNSGY) high-entropy ceramics and evaluated the fracture toughness of LNSGY, LZO and LCZ (Fig. 15). The fracture toughness of LNSGY ceramics was 2.0±0.3 $MPa{\cdot}m^{1/2}$, which was significantly higher than that of LZ (1.1±0.1 $MPa{\cdot}m^{1/2}$) and LCZ (1.4±0.1 $MPa{\cdot}m^{1/2}$). The high fracture toughness of LNSGY ceramics was related to the presence of ferroelastic domains. The doping of cations increased the strain field of the dislocations within the ceramics to increase the chances of crack bridging and deflection. In

addition, the high dislocation density inside the LNSGY ceramics increased the local plasticity of their surfaces, which promoted the stress release in the crack tip region and ultimately changed the direction of crack deflection.

6.3. Coefficient of thermal expansion

Since thermal barrier coatings operate in high-temperature environments, thermal expansion mismatches exist between the alloy substrate, the metal bond coat and the top coat [109]. When the difference in thermal expansion between different parts is too significant, an enormous thermal expansion mismatch stress will accumulate inside the coating, causing cracks to form inside the coating and leading to premature peeling of the coating, reducing the service life of the coating [110]. Therefore, there is a need to design materials for thermal barrier coatings with a high coefficient of thermal expansion (CTE).

According to the thermal expansion correlation theory, it is predicted that the CTE (α) of the material has negative correlation with the lattice energy U, the lattice energy is in positive correlation with the ionic bonding strength I, and the ionic bonding strength I is in positive correlation with the average electronegativity difference of anions ΔX. Hence, the thermal expansion coefficient shows negative correlation with the average electronegativity difference of anions [111–113]:

$$\alpha = \frac{b}{a + U} \tag{9}$$

$$U \propto I \tag{10}$$

$$I = 1 - e^{-\frac{1}{4}\Delta X^2} \tag{11}$$

$$\Delta X = \sqrt{\sum_{i=1}^{n} c_i \left(X_i - \sum_{i=1}^{n} c_i \cdot X_i \right)^2} \tag{12}$$

where n, c_i and X_i denote the total number of atoms, the molar fraction of the i element and the electronegativity of the i element, respectively. In addition, the lattice energy can also be calculated by [43]:

$$U = \frac{1.38942 \times 10^5 A \cdot Z_1 \cdot Z_2}{R_0} \left(1 - \frac{1}{n} \right) \tag{13}$$

where n is the Born index, A is the Madelung constant, Z_1 and Z_2 are the absolute values of the positive and negative ion charges, respectively, and R_0 is the positive and negative ion spacing. For high-entropy ceramics, element doping affects its thermal expansion coefficient in two ways [114]. Firstly, when the dopant element is a rare earth element, the lattice torsion, defects and disorder caused by the mutual solid solution of multi-component constituents will lead to a decrease in the strength of ionic bonding and increase the CTE of the high-entropy ceramics. Secondly, when the dopant element is a transition metal element, the positive-negative ion spacing R_0 will be decreased, which improves the lattice energy and decreases the thermal expansion coefficient. The increase in lattice energy has less effect on the coefficient of thermal expansion than lattice distortions, defects and disorder, so doping of transition elements still increases the coefficient of thermal expansion of ceramics.

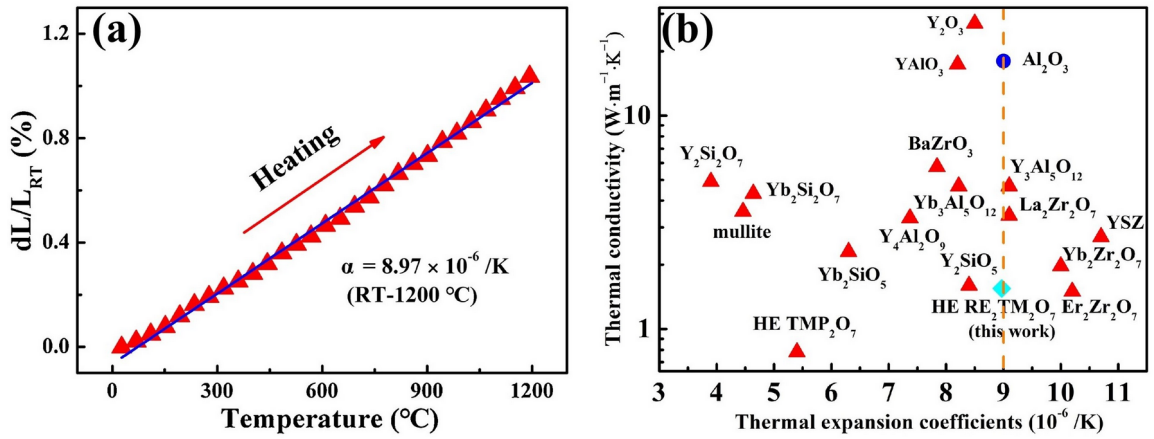

Figure 16. Linear thermal expansion curve measured by an optical dilatometer (a) and thermal conductivity versus thermal expansion coefficients (b) for $(Y_{0.25}Yb_{0.25}Er_{0.25}Lu_{0.25})_2(Zr_{0.5}Hf_{0.5})_2O_7$ together with selected TBC materials and Al_2O_3 [99]

$(Y_{0.25}Yb_{0.25}Er_{0.25}Lu_{0.25})_2(Zr_{0.5}Hf_{0.5})_2O_7$ high-entropy ceramics were prepared by discharge plasma sintering and their thermal expansion behaviour was analysed [99] (Fig. 16). The linear thermal expansion curve of the high-entropy ceramics was nearly linear. The average thermal expansion coefficient obtained from the slope was 8.97×10^{-6} 1/°C, which was lower than that of $Yb_2Zr_2O_7$ (10.7×10^{-6} 1/°C) and $Er_2Zr_2O_7$ (11.0×10^{-6} 1/°C), but close to Al_2O_3 (9.0×10^{-6} 1/°C). These findings suggested that high-entropy ceramics might be possible to reduce the mismatch of thermal expansion between TC and TGO in high-temperature

environments, potentially increasing the thermal cycle life of thermal barrier coatings.

$(La_{1/6}Nd_{1/6}Yb_{1/6}Y_{1/6}Sm_{1/6}Lu_{1/6})_2Ce_2O_7$ (HECeO) high-entropy ceramics was prepared by sol-gel method and its thermal expansion behaviour was compared with $Sm_2Ce_2O_7$ and YSZ (Fig. 17) [47]. The thermal expansion coefficients of HECeO ceramics were positively dependent on temperature and higher than those of $Sm_2Ce_2O_7$ and YSZ. The high thermal expansion coefficients of HECeO ceramics were related to their lower structural order and larger Re–O atomic distance.

6.4. Anti-sintering properties

As thermal barrier coatings accumulate a large amount of thermal stress in the working environment, the microcracks and pores inside the coating become the space for stress release [115]. Therefore, for ceramic materials, a higher resistance to sintering results in slower grain growth, increased content of microcracks and pores, and improved toughness and service life of the coating [116]. In addition to providing stress release space inside the coating, the presence of microcracks and pores can provide additional phonon scattering points, lowering the mean free path of phonon and optimizing the thermal insulation effect of the coating, so the sintering resistance has become an essential indicator for evaluating the performance of high-entropy ceramics [117]. For testing sintering resistance, coatings are evaluated by comparing porosity changes before and after high-temperature annealing, while ceramic green bodies are assessed by comparing grain size before and after high-temperature annealing.

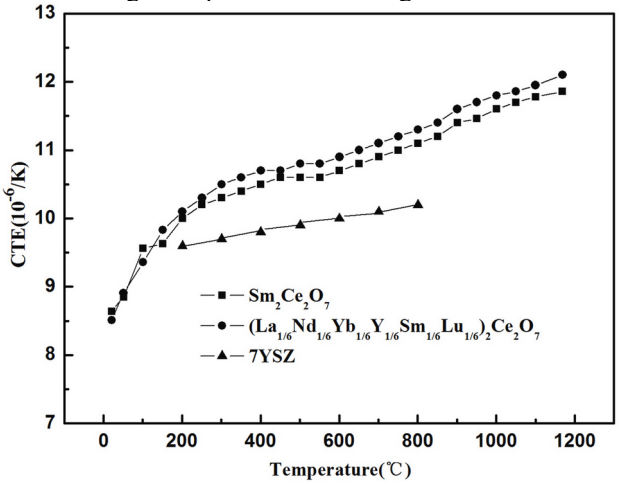

Figure 17. Coefficient of thermal expansion for high-entropy oxide [47]

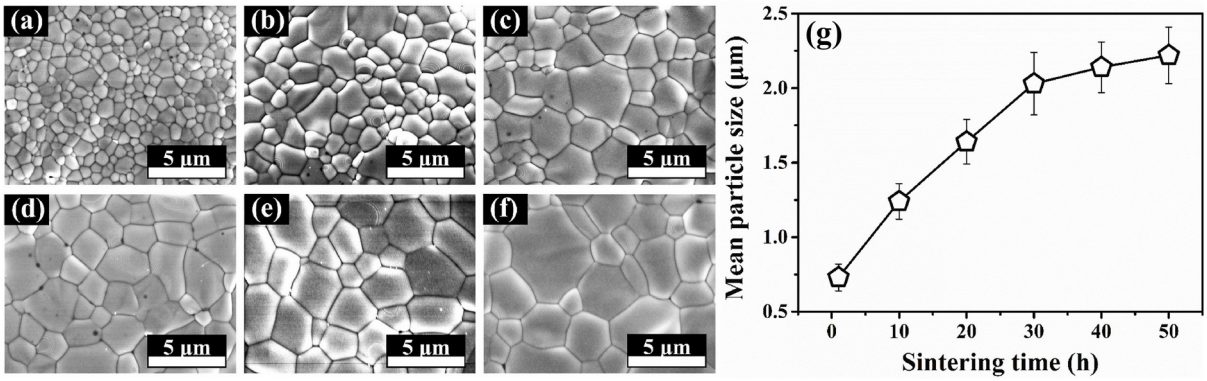

Figure 18. SEM images of $(Dy_{0.2}Nd_{0.2}Sm_{0.2}Eu_{0.2}Yb_{0.2})_2Zr_2O_7$ sample sintered at 1600 °C for: a) 1 h, b) 10 h, c) 20 h, d) 30 h, e) 40 h and f) 50 h, and mean particle size of the sample sintered at 1600 °C for 10-50 h [118]

The sintering resistance of zirconia-based ceramics may be enhanced by doping with Re^{3+}, which has a larger ionic radius. The researchers studied the impact of certain rare earth cations on the sintering resistance of the ceramics [118]: Dy can improve the sintering resistance of ZrO_2, Sm can inhibit the outward diffusion of cations in the ceramic lattice to improve the sintering resistance, Nd can provide oxygen vacancies as well as displace defects, promote the formation of defect clusters and inhibit the migration of grain boundaries to reduce sintering.

Luo *et al*. [118] investigated the sintering behaviour of $(Dy_{0.2}Nd_{0.2}Sm_{0.2}Eu_{0.2}Yb_{0.2})Zr_2O_7$ high-entropy ceramics at 1600 °C (Fig. 18). The grain size increased with the increasing holding time. When the sintering time was 10 h, the grain size of the high-entropy ceramic was 1.24 μm, which was 64% lower than that of $La_2Zr_2O_7$ (3.46 μm) under the same conditions. In addition, the average grain size of high-entropy ceramics sintered for 10–50 h increased only from 0.73 to 2.22 μm, and the average grain growth rate was only 0.026 μm/h, which was lower than that of ceramics such as $Yb_2Zr_2O_7$ (0.143 μm/h), $La_2Zr_2O_7$ (0.408 μm/h) and YSZ (0.654 μm/h).

$(Y_{0.2}Yb_{0.2}Lu_{0.2}Eu_{0.2}Er_{0.2})_3Al_5O_{12}$ (HEAlO) was prepared by using the solid-state reaction method [31]. They compared the sintering behaviour of HEAlO at 1590 °C with Y_2O_3, $Yb_2Zr_2O_7$ and $(Y_{0.25}Yb_{0.25}Er_{0.25}Lu_{0.25})_2(Zr_{0.5}Hf_{0.5})_2O_7$ (HEZHO). The results are shown in Fig. 19. The grain growth rate of HEAlO was significantly slower than that of HEZHO, $Yb_2Zr_2O_7$ and Y_2O_3 at the annealing temperature of

1590 °C. As the annealing time was increased from 1 to 18 h, the average grain size of HEAlO increased from 1.56 to 2.27 μm. In addition, the fitted grain growth rate of HEAlO was 0.038 $\mu m^2/h$, which was much lower than that of HEZHO, $Yb_2Zr_2O_7$ and Y_2O_3.

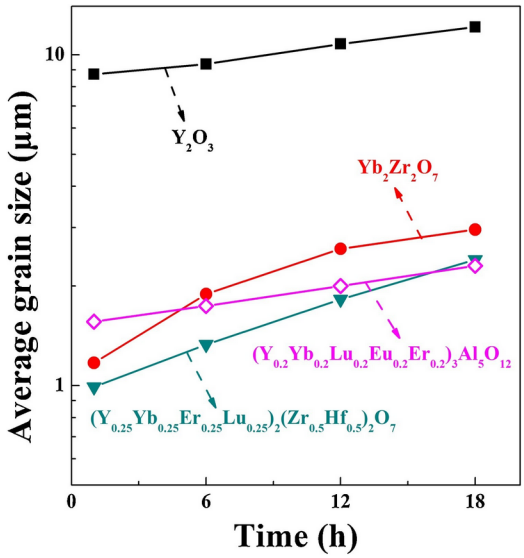

Figure 19. Comparison of average grain sizes of $(Y_{0.2}Yb_{0.2}Lu_{0.2}Eu_{0.2}Er_{0.2})_3Al_5O_{12}$ specimen with those of $(Y_{0.25}Yb_{0.25}Er_{0.25}Lu_{0.25})_2(Zr_{0.5}Hf_{0.5})_2O_7$, $Yb_2Zr_2O_7$ and Y_2O_3 [31]

6.5. Anti-corrosion properties

In a real working environment, thermal barrier coatings serve the purpose of providing thermal insulation and isolate the metal substrate from external corrosion. This is essential to prevent irreversible damage to the metal substrate from molten corrosive substances in high-temperature environments [119]. As a result, corrosion resistance has become a critical evaluation criterion for ceramic materials used in thermal barrier coatings.

The one of the two main reasons for corrosion of the thermal barrier coatings is CaO-MgO-Al_2O_3-SiO_2 (CMAS) corrosion. During the engine's operation, it absorbs dust particles from the external environment. These dust particles are mainly composed of CaO-MgO-Al_2O_3-SiO_2 and at temperatures higher than 1300 °C, they melt and infiltrate the coating internally [120]. CMAS corrosion damages thermal barrier coatings both thermochemically and thermodynamically [121]: i) in terms of thermochemical damage, CMAS reacts with the ceramic material, leading to its decomposition and loss of performance; ii) in terms of thermodynamic damage, the generation of corrosion products and the phase transition will cause a large amount of volume expansion within the coating, which accelerates the failure of the coating. Therefore, there is a need to develop ceramic materials with excellent resistance to CMAS corrosion to improve the service life and performance of thermal barrier coatings. Due to the slow diffusion effect and the “cocktail effect” of high-entropy ceramic materials, researchers have begun to search for high-entropy ceramic materials with

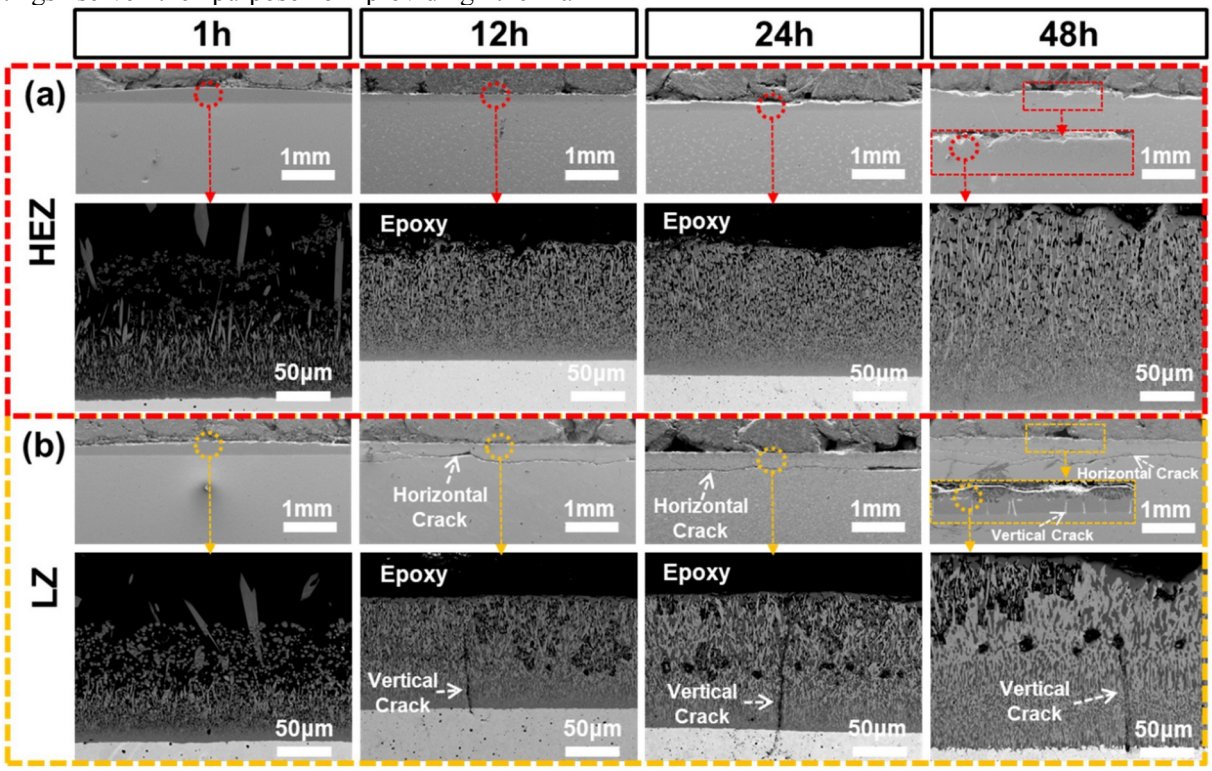

Figure 20. Low and high magnification SEM images of: a) HEZ and b) LZ after CMAS corrosion tests at 1300 °C for 1, 12, 24 and 48 h [122]

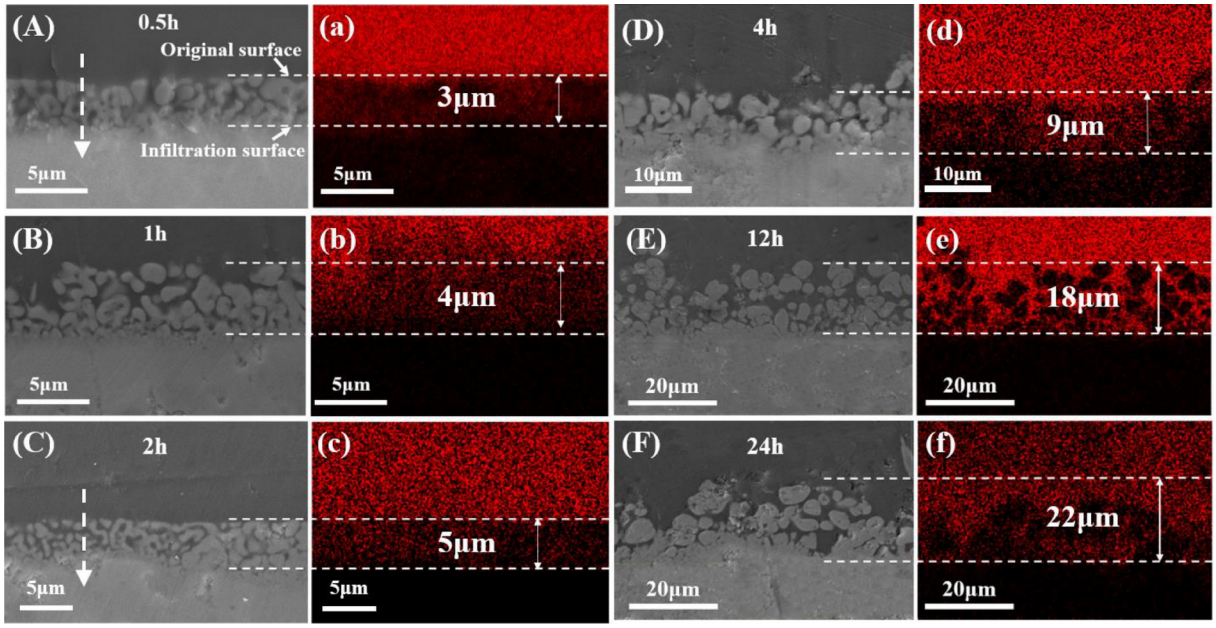

Figure 21. The cross-sectional images of CMAS-reacted HE-REZ pellets for 0.5, 1, 2, 4, 12, 24 h (A-F) and the corresponding EDS elemental Si maps (a-f) [123]

excellent resistance to CMAS corrosion. Tu *et al.* [122] prepared $(La_{0.2}Nd_{0.2}Sm_{0.2}Eu_{0.2}Gd_{0.2})_2Zr_2O_7$ high-entropy ceramics as well as $La_2Zr_2O_7$ single-component ceramics by the solid-state method and analysed the CMAS corrosion behaviours of the two ceramics in 1300 °C environment (Fig. 20). The high-entropy ceramics retained the intact structure after corrosion and a dense reaction layer appeared on the top. In contrast, many horizontal and vertical cracks appeared inside $La_2Zr_2O_7$. Vertical cracks provided penetration channels for the molten CMAS, which led to corrosion of the bottom ceramics, and the horizontal cracks led to the spalling of ceramic materials, which prevented them from being correctly applied to high-temperature environments. High-entropy ceramics can optimize the corrosion resistance in two aspects. Firstly, high-entropy ceramics have excellent CTE and low Young's modulus, which reduce the thermal stress inside the reaction layer and ceramic material under a high-temperature environment, avoid the formation of horizontal and vertical cracks, and prevent the external un-reacted CMAS from continuing to penetrate into the interior of the coating. Secondly, the high-entropy ceramics are composed of multi-component rare earth elements, thus, the slow diffusion effect not only slows down the dissolution of rare earth elements into CMAS, but also the doping of rare earth elements provides a specific stabilizing effect for zirconium oxide, avoiding the phase transformation in a high-temperature environment, reducing the internal stress in ceramics, and improving the corrosion resistance of the high-entropy ceramics.

Deng *et al.* [123] prepared $(Y_{0.2}Gd_{0.2}Er_{0.2}Yb_{0.2}Lu_{0.2})_2Zr_2O_7$ high-entropy ceramics by solid-state method and analysed its resistance to CMAS corrosion in 1300 °C environment, and the corrosion results are shown in Fig. 21. After 24 h of thermal corrosion, the high-entropy ceramics were only penetrated by 22 μm by molten CMAS. This was attributed to the larger radius of the doped rare-earth cations. The apatite formed by reaction with CMAS effectively filled the internal pores of the coating, reducing the CMAS penetration rate to 0.793 μm/h. As a result, the high-entropy ceramics exhibited good resistance to CMAS corrosion.

$(Y_{0.2}Dy_{0.2}Er_{0.2}Tm_{0.2}Yb_{0.2})_4Hf_3O_{12}$ high-entropy ceramics was obtained by the UHS method and their CMAS corrosion resistance as well as their CMAS wetting behaviour at 1300 °C were investigated [124]. In terms of the corrosion mechanism, the high-entropy apatite phase generated during the reaction process improved the densification of the reaction layer, making the reaction layer a barrier for preventing the penetration of molten CMAS and effectively reducing the thickness of the reaction layer. In terms of CMAS wetting behaviour, the molten CMAS on the surface of high-entropy ceramics had a larger contact angle than that on the conventional YSZ, which was conducive to improving the high-temperature corrosion resistance of high-entropy ceramics.

In addition to the CMAS corrosion, another important type of corrosion of thermal barrier coatings is Na_2SO_4+V_2O_5 corrosion. Bahamirian *et al.* [125] analysed the residual material on the surface of turbine engine blades. They found that Na_2SO_4 and V_2O_5 exhibit deposition on hot-end components when the engine is running on low-grade fuel. The two salts react in high-temperature environments to form $NaVO_3$, which reacts with the rare earth oxides doped in the ceramic material and causes the coating to

decompose [126]. Compared with CMAS, Na_2SO_4 and V_2O_5 have lower melting points and react with thermal barrier coatings below 1000 °C, and the mobility, corrosion process, and corrosion rate change with temperature [127]. Currently, there are limited studies on the corrosion resistance of high-entropy ceramic materials against Na_2SO_4+V_2O_5. Therefore, the corrosion resistance can only be inferred from the high-entropy effect as well as from the corrosion resistance of zirconia doped with poly-rare earth oxides.

First of all, high-entropy ceramics exhibit the "cocktail" effect. Despite rare earth oxides being fully dissolved in the lattice of high-entropy ceramics, they still maintain their oxide properties. This means that their acidity can be determined based on the ionic radius of the element and the order of reaction of the rare earth oxides with $NaVO_3$ can be analysed according to the Lewis acid-base mechanism [128]. Song *et al*. [129] analysed the reaction process of Gd_2O_3-Yb_2O_3-Y_2O_3 co-doped ZrO_2 with $NaVO_3$. They discovered that Gd_2O_3 has the strongest alkaline character and would react first with the molten corrosion, while Yb_2O_3 and Y_2O_3 would remain to stabilize ZrO_2 and prevent it from undergoing a phase transition. This suggests that high-entropy ceramics containing multi-component rare earth oxides can be stabilized by sacrificing the alkalinity of the strongest rare earth oxide while retaining the others, thus enhancing the resistance of the coating to high-temperature corrosive environments. Therefore, high-entropy ceramics with multi-component rare earth oxides can optimize the corrosion resistance of coatings by sacrificing highly alkaline rare earth oxides and preserving other rare earth elements to stabilize zirconia, prevent phase transformation and minimize consumption of corrosive materials under high-temperature corrosive conditions.

6.6. High-temperature phase stability

Under high-temperature thermal exposure environments, the thermal barrier coating properties change not only at the interface location but also inside the ceramic material. Conventional YSZ has a transition process of the *t′* phase transforming into the *t* and *c* phases during long-term treatment [130]. When the temperature is higher than 1200 °C, the phase stability of YSZ will further decrease, the *t* phase will be transformed into the *m* phase, and a mixture of *t* + *m* + *c* phases will be formed at the defect location of Y_2O_3 [131]. The phase transformation of YSZ will lead to volume changes and structural destabilization of the ceramic coating, which will affect its service life [132]. Therefore, it is essential to characterize the high-temperature phase stability of high-entropy ceramics.

$(La_{0.2}Nd_{0.2}Gd_{0.2}Sm_{0.2}Pr_{0.2})MgAl_{11}O_{19}$ (HELMA) high-entropy ceramics was prepared by solid-state reaction method and its high-temperature phase stability was characterized [133]. The results show that the HELMA ceramics remains a single-phase solid solution after annealing at 1400 °C for 2 h, indicating that HELMA has good high-temperature phase stability. Liu *et al*. [134] prepared $(Dy_{0.2}Ho_{0.2}Er_{0.2}Tm_{0.2}Lu_{0.2})_2Hf_2O_7$ ceramics by discharge plasma sintering and characterized their high-temperature phase stability. The TG-DSC curves are shown in Fig. 22. There was no sign of mass loss or any exothermic/endothermic peaks in the range of room temperature to 1500 °C, which proved that $(Dy_{0.2}Ho_{0.2}Er_{0.2}Tm_{0.2}Lu_{0.2})_2Hf_2O_7$ ceramics have excellent phase stability in the 1500 °C range.

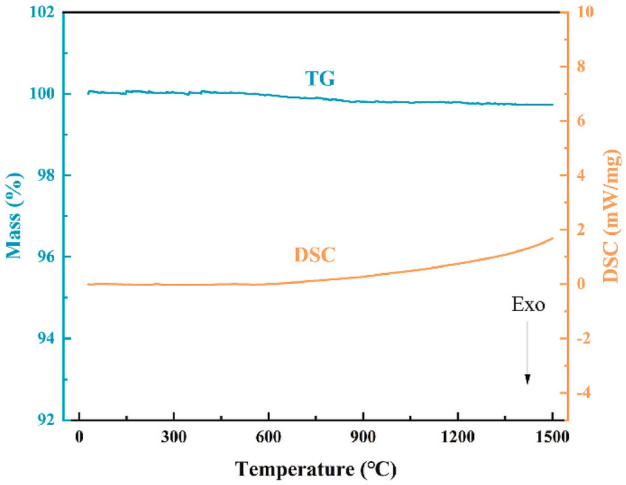

Figure 22. TG-DSC curves of $(Dy_{0.2}Ho_{0.2}Er_{0.2}Tm_{0.2}Lu_{0.2})_2Hf_2O_7$ as a function of temperature [134]

6.7. Chemical compatibility

During the practical application of thermal barrier coatings, elements such as Al, Ni, Cr, and Co inside the bond coat oxidize and form TGO between the bond coat and the top coat. Since Al_2O_3 inside the TGO may react with ceramic materials in a high-temperature environment and affect the service life of thermal barrier coatings, it is necessary to investigate the high-temperature chemical compatibility of high-entropy ceramic materials with Al_2O_3.

$(La_{0.2}Ce_{0.2}Nd_{0.2}Sm_{0.2}Eu_{0.2})PO_4$ powder was mixed with Al_2O_3 powder and annealed at 1600 °C [51]. The XRD pattern of the mixed powder at the end of the holding time is shown in Fig. 23. Only the diffraction peaks of $(La_{0.2}Ce_{0.2}Nd_{0.2}Sm_{0.2}Eu_{0.2})PO_4$ and Al_2O_3 phases were detected and no diffraction peaks of other substances appeared, indicating that this high-entropy ceramics has excellent chemical compatibility with Al_2O_3.

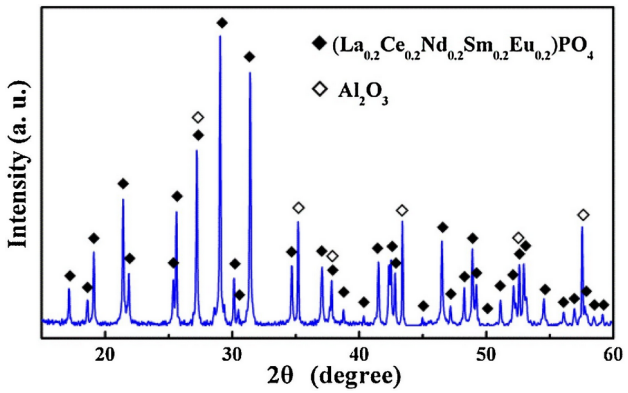

Figure 23. XRD pattern of the mixed powders of HE $(La_{0.2}Ce_{0.2}Nd_{0.2}Sm_{0.2}Eu_{0.2})PO_4$ and Al_2O_3 in equivalent volume ratio after annealing at 1600 °C for 1 h [51]

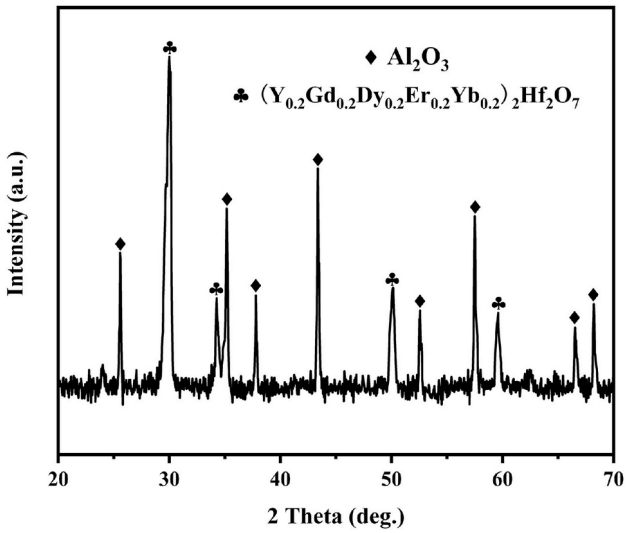

Figure 24. XRD pattern of $(Y_{0.2}Gd_{0.2}Dy_{0.2}Er_{0.2}Yb_{0.2})_2Hf_2O_7/Al_2O_3$ mixed powders after annealing at 1300 °C for 4 h [135]

$(Y_{0.2}Gd_{0.2}Dy_{0.2}Er_{0.2}Yb_{0.2})_2Hf_2O_7$ high-entropy powder was prepared by solution combustion method and mixed with Al_2O_3 before heating at 1300 °C for 4 h [135]. Only the diffraction peaks of the high-entropy ceramics and Al_2O_3 (Fig. 24) were observed in the annealed powder, indicating that the two powders did not react in the high-temperature environment. This confirms the excellent high-temperature chemical compatibility of this high-entropy ceramics.

Current research on chemical compatibility of high-entropy ceramics focuses on Al_2O_3, which is only a first-stage oxidation product of the bond coat during isothermal oxidation of the thermal barrier coating. When the Al element inside the metal bond coat is consumed in large quantities, the bond coat starts to undergo the second oxidation stage. The oxygen reacts with the elements inside the bonding layer, such as Ni, Cr and Co. The generated oxide clusters will diffuse to the interface between the TGO and ceramic layer, so the metal oxides, such as Ni, Cr and Co, need to be considered for checking the chemical compatibility of high-entropy ceramic materials.

VII. Summary and outlook

With the continuous development of aerospace technology, the increasing temperature of the engine inlet puts higher demands on the performance of ceramic materials for thermal barrier coatings, thus requiring the development of ceramic materials with lower thermal conductivity, better corrosion resistance, better high-temperature phase stability, and better thermomechanical properties. High-entropy oxide ceramics, as a new type of materials with unique properties, are considered to be a thermal barrier coating material with excellent application prospects. This review highlighted the compositional design theory, synthesis methods, sintering methods and performance characteristics of high-entropy ceramics.

Beyond the material design, the following aspects need to be considered when using high-entropy ceramics as the top coat of the thermal barrier coatings: i) consider the compositional changes of trace elements within the ceramics during the thermal spraying process, ii) consider the structural changes during the thermal spraying process, such as the transformation of the pyrochlore structure to the defective fluorite structure and iii) select the appropriate coating preparation method based on the properties of high-entropy ceramics and develop the corresponding coating preparation process.

Based on the above studies, high-entropy ceramics are expected to be candidates for future ultrahigh-temperature thermal barrier coatings and replace the conventional YSZ ceramic coat. However, there are still some critical issues need to be solved in future research:

- Currently, high-entropy ceramic materials applied to thermal barrier coatings are all mixed with multiple components in equimolar or near-equimolar ratios. Explorations of various doping compositions, elemental combinations and microstructural designs to optimize thermal conductivity, coefficient of thermal expansion (CTE), CMAS resistance, mechanical properties and sintering resistance are crucial.
- High-entropy ceramics is a complex multi-dimensional scale coupling system. The existing basic theory cannot accurately describe the relationship between the internal composition, organization, structure and performance of high-entropy ceramics, and the deep-level mechanism research is still unclear. In recent years, with the development of computers and the improvement of computing power, the rapid development of materials computational science has pushed the development of high-entropy ceramics towards a

computationally-driven research and development paradigm. Therefore, combining the design and development of high-entropy ceramics with artificial intelligence is a future prospect.

- The future application of high-entropy ceramics in thermal barrier coatings should not be limited to designing the composition of high-entropy ceramics. It should also include optimizing the powder synthesis process to meet environmental requirements for specific ceramic material properties. Additionally, the synthesis of ceramic materials with high purity, controlled powder size and other necessary factors should be adequately carried out to ensure successful application in high-temperature and complex environments.

Acknowledgement: The authors are thankful for the support of the National Natural Science Foundation of China (No. 51702145) and the National Natural Science Foundation of China (No. 52371066).

References

1. Y. Long, Y.Z. Wang, X.H. Chen, R.X. Sang, "3D numerical reconstruction and microstructure regulation of thermal barrier coatings for high temperature components of gas turbine", *Ceram. Int.*, **47** [14] (2021) 20126–20140.
2. J.B. Fan, Q.S. Wang, X.J. Ning, Z.N. Sun, "Failure mechanisms for Gd_2O_3-Yb_2O_3 co-doped YSZ thermal barrier coatings under high-temperature gradient", *Ceram. Int.*, **50** [16] (2024) 28563–28572.
3. M. Bogdan, I. Peter, "A comprehensive understanding of thermal barrier coatings (TBCs): applications, materials, coating design and failure mechanisms", *Metals*, **14** (2024) 575.
4. K. Mondal, L. Nunez, C.M. Downey, I.J. van Rooyen, "Thermal barrier coatings overview: Design, manufacturing, and applications in high-temperature industries", *Ind. Eng. Chem. Res.*, **60** [17] (2021) 6061–6077.
5. P. Jiang, F. Sun, Y.W. Chen, D.J. Li, "Oxide growth in high-strain tolerance thermal barrier coating with segmented vertical cracks", *Ceram. Int.*, **50** [14] (2024) 25025–25033.
6. M.Q. Dai, Y.X. Xu, F. Peng, X.M. Song, Y.Z. Wang, W. Zheng, Y.L. Huang, Y. Zeng, "Influence of doping elements on thermo-physical properties of co-doped strontium zirconate for potential thermal barrier coatings", *J. Alloys Compd.*, **988** (2024) 174343.
7. X.Z. Li, W.X. Zhang, X.B. Cai, H.T. Liu, X.T. Luo, "High temperature hardness and thermal analysis of CoNiCrAlY alloys used as bond coats for thermal barrier coatings", *J. Mater. Res. Technol.*, **30** (2024) 1020–1023.
8. K.Y. Lü, L.H. Deng, Y. Huang, G. Li, J.N. Jiang, S.J. Dong, X.Q. Cao, "$Lu_4Hf_3O_{12}$ ceramics as potential top-coat materials for thermal/environmental barrier coatings", *Ceram. Int.*, **49** [18] (2023) 30892–30896.
9. Y.J. Chai, X.W. Yang, Y.M. Li, "Growth prediction and interlayer stress evolution of double-layered TGO in breakaway oxidation of thermal barrier coating system", *Surf. Coat. Technol.*, **458** (2023) 129348.
10. X.Z. Li, W.X. Zhang, X. B. Cai, "Mechanical evaluation of thermal barrier coatings by indentation: A review", *J. Mater. Res. Technol.*, **30** (2024) 5402–5416.
11. X.Y. Liu, P. Zhang, Y. Lu, G.H. Liu, J. Sun, W. Liu, W. Pan, C.L. Wan, "The microstructure and property evolution of $LaYbZr_2O_7$ thermal barrier coatings", *Surf. Coat. Technol.*, **471** (2023) 129928.
12. Z.L. Xue, L. Zhou, M.C. Shi, Z.Y. Zhang, E. Byon, S.H. Zhang, "Preparation and sintering behavior of GdYb-YSZ nanostructured thermal barrier coating", *J. Mater. Res. Technol.*, **26** (2023) 7237–7247.
13. D.L. Liu, R.D. Mu, L.M. He, S. Li, W.H. Yang, "Failure behaviour of EB-PVD YSZ thermal barrier coatings under simulated aero-engine operating conditions", *Surf. Coat. Technol.*, **474** (2023) 130027.
14. Z.Y. Shen, Z. Liu, G.X. Liu, R.D. Mu, L.M. He, J.W. Dai, "GdYbZrO thermal barrier coatings by EB-PVD: Phase, microstructure, thermal properties and failure", *Surf. Interfaces*, **24** (2023) 101123.
15. J.S. Wang, Y.H. Wang, X.J. Lu, M.Q. Hu, M.D. Chen, C.X. Shu, H. Zhang, Y.S. Tian, B. Liu, Q.S. Jing, "Comparison of corrosion behaviors and wettability of CMAS on Ta_2O_5-Y_2O_3 co-stabilized ZrO_2 and YSZ thermal barrier coatings", *J. Eur. Ceram. Soc.*, **43** [13] (2023) 5636–5651.
16. R.J. Alroy, K. Praveen, J. Joardar, D.S. Rao, G. Sivakumar, "Understanding the thermal barrier performance of plasma-sprayed rare-earth zirconate coating against volcanic ash ingestion", *Surf. Coat. Technol.*, **446** (2022) 128745.
17. M. Mikuskiewicz, D. Migas, G. Moskal, "Synthesis and thermal properties of zirconate, hafnate and cerate of samarium", *Surf. Coat. Technol.*, **354** (2018) 66–75.
18. M. Heleena, S.S. Kumar, N. Balaji, S.T. Aruna, "Solution combustion synthesized micron sized yttrium aluminum garnet ($Y_3Al_5O_{12}$) powder: A promising feedstock source for plasma spraying", *Ceram. Int.*, **48** [23] (2022) 35740–35749.
19. K.Y. Lü, S.J. Dong, Y. Huang, G. Li, J.N. Jiang, L.H. Deng, X.Q. Cao, "Influence of post heat treatment on the high-temperature performances of multi-layered thermal/environmental barrier coatings on SiC-based composites", *Ceram. Int.*, **49** [17] (2023) 28130–28141.
20. J.W. Yeh, S.K. Chen, S.J. Lin, J.Y. Gan, T.S. Chin, T.T. Shun, C.H. Tsau, S.Y. Chang, "Nanostructured high-entropy alloys with multiple principal elements: Novel alloy design concepts and outcomes", *Adv. Eng. Mater.*, **6** [5] 299–303.
21. C.M. Rost, E. Sachet, T. Borman, A. Moballegh, E.C. Dickey, D. Hou, J.L. Jones, S. Curtarolo, J.P. Maria, "Entropy-stabilized oxides", *Nat. Commun.*, **6** (2015) 8485.
22. Y.W. Ding, K.J. Ren, C. Chen, L. Huan, R.L. Gao, X.L. Deng, G. Chen, W. Cai, C.L. Fu, Z.H. Wang, X. Lei, "High-entropy perovskite ceramics: Advances in structure and properties", *Process. Appl. Ceram.*, **18** [1] (2024) 1–11.
23. J.H. Liu, Z. Lv, Y.W. Zhou, Z.W. Xie, H. Chen, L. Cheng, "Research progress of high-entropy ceramics materials for thermal barrier coatings", *Mater. Rep.*, **37** (2023) 84–94.

24. A.R. Mazza, E. Skoropata, Y. Sharma, J. Lapano, T.W. Heitmann, B.L. Musico, V. Keppens, Z. Gai, J.W. Freeland, T.R. Charlton, M. Brahlek, A. Morea, E. Dagotto, T.Z. Ward, "Designing magnetism in high entropy oxides", *Adv. Sci.*, **9** [10] 2200391.
25. Y.P. Zhang, X.Z. Chen, S. Jayalakshmi, R.A. Singh, V.B. Deev, E.S. Prusov, "Factors determining solid solution phase formation and stability in $CoCrFeNiX_{0.4}$ (X=Al, Nb, Ta) high entropy alloys fabricated by powder plasma arc additive manufacturing", *J. Alloys Compd.*, **857** (2021) 157625.
26. S. Acharya, J. Hwang, K. Kim, J. Kim, W. Hwang, A. Soon, W. Kim, "Quasi-random distribution of distorted nanostructures enhances thermoelectric performance of high-entropy chalcopyrite", *Nano Energy*, **112** (2023) 108493.
27. A. Nisar, C. Zhang, B. Boesl, A. Agarwal, "A perspective on challenges and opportunities in developing high entropy-ultra high temperature ceramics", *Ceram. Int.*, **46** [16] (2020) 25845–25853.
28. T.Q. Wen, S.S. Ning, D. Liu, B.L. Ye, H.H. Liu, Y.H. Chu, "Synthesis and characterization of the ternary metal diboride solid-solution nanopowders", *J. Am. Ceram. Soc.*, **102** [8] (2019) 4956–4962.
29. J. Gild, Y. Zhang, T. Harrington, S. Jiang, T. Hu, M.C. Quinn, W.M. Mellor, N. Zhou, K. Vecchio, J. Luo, "High-entropy metal diborides: A new class of high-entropy materials and a new type of ultrahigh temperature ceramics", *Sci. Rep.*, **6** (2016) 37946.
30. S.C. Jiang, T. Hu, J. Gild, N.X. Zhou, J.Y. Nie, M.D. Qin, T. Harrington, K. Vecchio, J. Luo, "A new class of high-entropy perovskite oxides", *Scr. Mater.*, **142** (2018) 116–120.
31. H. Chen, Z.F. Zhao, H.M. Xiang, F.Z. Dai, W. Xu, K. Sun, J.C. Liu, Y.C. Zhou, "High entropy $(Y_{0.2}Yb_{0.2}Lu_{0.2}Eu_{0.2}Er_{0.2})_3Al_5O_{12}$: A novel high temperature stable thermal barrier material", *J. Mater. Sci. Technol.*, **48** (2020) 57–62.
32. P. Sarker, T. Harrington, C. Toher, C. Oses, M. Samiee, J.P. Maria, D.W. Brenner, K.S. Vecchio, S. Curtarolo, "High-entropy high-hardness metal carbides discovered by entropy descriptors", *Nat. Commun.*, **9** (2018) 4980.
33. T.J. Harrington, J. Gild, P. Sarker, C. Toher, C.M. Rost, O.F. Dippo, C. McElfresh, K. Kaufmann, E. Marin, L. Borowski, P.E. Hopkins, J. Luo, S. Curtarolo, D.W. Brenner, K.S. Vecchio, "Phase stability and mechanical properties of novel high entropy transition metal carbides", *Acta Mater.*, **166** (2019) 2019.
34. Y. L. Yu, P. Zhang, X.Y. Liu, G.H. Liu, J. Sun, W. Liu, W. Pan, C.L. Wan, "Effect of feedstock powder size on the microstructure and thermal conductivity of quasi-eutectic $LaYbZr_2O_7$ TBCs", *Ceram. Int.*, **50** [8] (2024) 13684–13689.
35. M. Cvetnic, R. Splajt, E. Topic, M. Rubcic, N. Bregovic, "Direct thermodynamic characterization of solid-state reactions by isothermal calorimetry", *Phys. Chem. Chem. Phys.*, **26** [1] (2023) 67–75.
36. Y.C. Du, Z. Hua, F. Liang, Y.M. Li, Y.N. Dai, Y.C. Yao, "Synthesis of lithium iron phosphate cathode material by liquid state method", *Prog. Chem.*, **29** [1] 137–148.
37. A. Kumar, S. Dutta, S. Kim, T. Kwon, S.S. Patil, N. Kumari, S. Jeevanandham, I.S. Lee, "Solid-state reaction synthesis of nanoscale materials: Strategies and applications", *Chem. Rev.*, **122** [15] (2024) 12748–12863.
38. M. Chaika, W. Paszkowicz, W. Strek, D. Hreniak, R. Tomala, N. Sfronova, A. Doroshenko, S. Parkhomenko, P. Dluzewski, M. Kozlowski, O. Vovk, "Influence of Cr doping on the phase composition of Cr,Ca:YAG ceramics by solid state reaction sintering", *J. Am. Ceram. Soc.*, **102** [4] (2019) 2104–2115.
39. X. Wang, L. Zhang, Y.Q. Ji, J. Chu, P.F. Pan, S.Q. Pan, H.L. Wang, L. Wang, M. Zhang, "$Gd_2Zr_2O_7$ ceramics synthesized by solid-state reactive sintering: Effects of starting powders with different-scale particle sizes", *Ceram. Int.*, **48** [12] (2022) 16839–16844.
40. T.K. Mac, T.T. Ta, H.T. Nguyen, N. Van Hoang, T.L.H. Pham, V. Duong, A.T.T. Pham, B.T. Phan, S.L. Cho, A.T. Duong, "The impact of sintering temperature on the thermoelectric performance of Cu_2Se synthesized by solid state reaction method", *J. Solid State Chem.*, **322** (2023) 123998.
41. K.C. Kumar, N.M. Rao, S. Kaleemulla, G.V. Rao, "Structural, optical and magnetic properties of Sn doped ZnS nano powders prepared by solid state reaction", *Phys. B*, **522** (2017) 75–80.
42. H. Zhan, W. Ma, X.X. Han, W.C. Liang, J.J. Hao, H.Y. Dong, Y. Bai, H.X. Liu, X.F. Meng, "A new type of $Sr(Zr_{0.2}Hf_{0.2}Ce_{0.2}Yb_{0.2}Me_{0.2})O_{3-x}$ (Me = Y, Gd) high-entropy ceramics used in thermal barrier coatings", *Int. J. Appl. Ceram. Technol.,* **20** [3] (2023) 1764–1773.
43. Y.H. Zhang, M. Xie, Z.G. Wang, R.D. Mu, X.W. Song, Y.B. Yu, J.X. Bao, F. Zhou, W. Pan, "Marked reduction in the thermal conductivity of $(La_{0.2}Gd_{0.2}Y_{0.2}Yb_{0.2}Er_{0.2})_2Zr_2O_7$ high-entropy ceramics by substituting Zr^{4+} with Ti^{4+}", *Ceram. Int.*, **48** [7] (2022) 9602–9609.
44. M.Q. Yao, Y.H. Wei, L.Q. Hu, B.S. Xu, "Fabrication of nanometer powders by the sol-gel method", *Rare Met. Mater. Eng.*, **31** [5] (2002) 325–329.
45. F. Li, X. Huang, J.X. Liu, G.J. Zhang, "Sol-gel derived porous ultra-high temperature ceramics", *J. Adv. Ceram.*, **9** [1] (2020) 1–16.
46. X.S. Zhang, L.Y. Xue, F. Yang, Z.H. Shao, H. Zhang, Z.G. Zhao, K.X. Wang, "$(La_{0.2}Y_{0.2}Nd_{0.2}Gd_{0.2}Sr_{0.2})CrO_3$: A novel conductive porous high-entropy ceramic synthesized by the sol-gel method", *J. Alloys Compd.*, **863** (2021) 158763.
47. H.S. Zhang, L.M. Zhao, W.W. Sang, X.G. Chen, A. Tang, H.M. Zhang, "Thermophysical performances of $(La_{1/6}Nd_{1/6}Yb_{1/6}Y_{1/6}Sm_{1/6}Lu_{1/6})_2Ce_2O_7$ high-entropy ceramics for thermal barrier coating applications", *Ceram. Int.*, **48** [2] (2022) 1512–1521.
48. S. Akrami, P. Edalati, M. Fuji, K. Edalati, "High-entropy ceramics: Review of principles, production and applications", *Mater. Sci. Eng., R*, **146** (2021) 100644.
49. L. Nadaraia, N. Jalabadze, R. Chedia, L. Khundadze, "Production of nanopowder and bulk aluminate ceramic scintillators", *Ceram. Int.,* **39** [3] (2013) 2207–2214.
50. Z.F. Zhao, H.M. Xiang, F.Z. Dai, Z.J. Peng, Y.C. Zhou, "$(La_{0.2}Ce_{0.2}Nd_{0.2}Sm_{0.2}Eu_{0.2})_2Zr_2O_7$: A novel high-entropy ceramic with low thermal conductivity and sluggish grain growth rate", *J. Mater. Sci. Technol.*, **35** [11] 2647–2651.

51. Z.F. Zhao, H. Chen, H.M. Xiang, F.Z. Dai, X.H. Wan, Z.J. Peng, Y.C. Zhou, "$(La_{0.2}Ce_{0.2}Nd_{0.2}Sm_{0.2}Eu_{0.2})PO_4$: A high-entropy rare-earth phosphate monazite ceramic with low thermal conductivity and good compatibility with Al_2O_3", *J. Mater. Sci. Technol.*, **35** [12] (2019) 2892–2896.
52. E. Novitskaya, J.P. Kelly, S. Bhaduri, O.A. Graeve, "A review of solution combustion synthesis: an analysis of parameters controlling powder characteristics", *Int. Mater. Rev.*, **66** [3] (2021) 188–214.
53. A.Q. Mao, H.Z. Xiang, Z.G. Zhang, K. Kuramoto, H.Y. Yu, SL. Ran, "Solution combustion synthesis and magnetic property of rock-salt $(Co_{0.2}Cu_{0.2}Mg_{0.2}Ni_{0.2}Zn_{0.2})O$ high-entropy oxide nanocrystalline powder", *J. Magn. Magn. Mater.*, 484 (2019) 245–252.
54. F.T. Li, J.R. Ran, M. Jaroniec, S.Z. Qiao, "Solution combustion synthesis of metal oxide nanomaterials for energy storage and conversion", *Nanoscale*, **7** [42] (2015) 17590–17610.
55. E.A.C. Miranda, J.F.M. Carvajal, O.J.R. Baena, "Effect of the fuels glycine, urea and citric acid on synthesis of the ceramic pigment $ZnCr_2O_4$ by solution combustion", *Mater. Res-Ibero-Am. J.*, **18** [5] (2015) 1038–1043.
56. A.V. Saghir, S.M. Beidokhti, J.V. Khaki, A. Salimi, "One-step synthesis of single-phase (Co,Mg,Ni,Cu,Zn)O High entropy oxide nanoparticles through SCS procedure: Thermodynamics and experimental evaluation", *J. Eur. Ceram. Soc.*, **41** [1] (2021) 563–579.
57. K.B. Zhang, W.W. Li, J.J. Zeng, T. Deng, B.Z. Luo, H.B. Zhang, X.G. Huang, "Preparation of $(La_{0.2}Nd_{0.2}Sm_{0.2}Gd_{0.2}Yb_{0.2})_2Zr_2O_7$ high-entropy transparent ceramic using combustion synthesized nanopowder", *J. Alloys Compd.*, **817** (2020) 153328.
58. K.T. Pasupuleti, K. Vattappara, S.A. Gomes, P. Ramaswamy, "Thermal fatigue characteristics of $8Y_2O_3$-ZrO_2, $La_2Zr_2O_7$, $La_2(Zr_{0.7}Ce_{0.3})_2O_7$ and $La_2Ce_2O_7$ thermal barrier coatings in duplex, multilayer functionally graded and multilayer configurations", *Process. Appl. Ceram.*, **17** [3] (2023) 236–247.
59. Z.H. Liu, H.B. Yang, Y.F. Jia, X. Shu, "Heat protective properties of NiCrAlY/Al_2O_3 gradient ceramic coating fabricated by plasma spraying and slurry spraying", *Surf. Coat. Technol.*, **327** (2017) 1–8.
60. Y. Xue, H.X. Zhang, X.Q. Zhao, Y.L. An, G. Liu, Y.C. Ma, H.X. Li, H.D. Zhou, J.M. Chen, "Enhanced thermal shock resistance of gradient high-entropy $(La_{0.2}Nd_{0.2}Sm_{0.2}Eu_{0.2}Gd_{0.2})_2Ce_2O_7$/YSZ thermal barrier coatings", *Ceram. Int.*, **50** [10] (2024) 18024–18034.
61. Y. Ma, X.B. Zhao, F.Y. Hong, K. Yang, "The influence of the elemental valence on the thermophysical properties of high entropy $(La_{0.2}Sm_{0.2}Eu_{0.2}Yb_{0.2}Y_{0.2})_2(Ce_{0.5}Zr_{0.5})_2O_7$ coatings for thermal barrier application", *Ceram. Int.*, **50** [23] (2024) 51410–51420.
62. L.D. Zhu, P.S. Xue, Q. Lan, G.R. Meng, Y. Ren, Z.C. Yang, P.H. Xu, Z. Liu, "Recent research and development status of laser cladding: A review", *Opt. Laser Technol.*, **138** (2021) 106915.
63. K.M. Wang, Z.L. Zhang, D.D. Xiang, J. Ju, "Research and progress of laser cladding: process, materials and applications", *Coatings*, **12** [10] (2022) 1382.
64. P.F. Zhao, Z.M. Shi, X.F. Wang, Y.Z. Li, Z.Y. Cao, M.D. Zhao, J.H. Liang, "A review of the laser cladding of metal-based alloys, ceramic-reinforced composites, amorphous alloys, and high-entropy alloys on aluminum alloys", *Lubricants*, **11** [11] (2023) 482.
65. D.B. Zhang, X.L. Feng, R.Q. Song, N. Wang, Y.S. Zhang, "Investigation on bi-layer coating with $La_2(Ti_{0.2}Zr_{0.2}Sn_{0.2}Ce_{0.2}Hf_{0.2})_2O_7$/YSZ prepared by laser cladding", *Ceram. Int.*, **49** [7] (2023) 10525–10534.
66. I.W. Chen, X.H. Wang, "Sintering dense nanocrystalline ceramics without final-stage grain growth", *Nature*, **404** [6774] (2000) 168–171.
67. S.L. Tan, X.M. Zhang, Z.P. Zhao, Z.Z. Wu, "Driving force evolution in solid-state sintering with coupling multiphysical fields", *Ceram. Int.*, **46** [8] (2020) 11584–11592.
68. R.M. Cannon, W.C. Carter, "Interplay of sintering microstructures, driving forces, and mass transport mechanisms", *J. Am. Ceram. Soc.*, **72** [8] (1989) 1550–1555.
69. M.M. Gong, R.H.R. Castro, F. Liu, "Modeling the final sintering stage of doped ceramics: mutual interaction between grain growth and densification", *J. Mater. Sci.*, **53** [3] (2018) 1680–1698.
70. F. Li, L. Zhou, J.X. Liu, Y.C. Liang, "High-entropy pyrochlores with low thermal conductivity for thermal barrier coating materials", *J. Adv. Ceram.*, **8** [4] (2020) 576–582.
71. X.C. Cai, S.J. Ding, Z.J. Li, X. Zhang, K.K. Wen, L.D. Xu, Y. Zhang, Y. Peng, T.D. Shen, "Simultaneous sintering of low-melting-point Mg with high-melting-point Ti via a novel one-step high-pressure solid-phase sintering strategy", *J. Alloys Compd.*, **858** (2021) 158344.
72. C.W. Wang, W.W. Ping, Q. Bai, H.C. Cui, R. Hensleigh, R.L. Wang, A.H. Brozena, Z.P. Xu, J.Q. Dai, Y. Pei, C.L. Zheng, G. Pastel, J.L. Gao, X.Z. Wang, H. Wang, J.C. Zhao, B. Yang, X.Y. Zheng, J. Luo, Y.F. Mo, B. Dunn, L.B. Hu, "A general method to synthesize and sinter bulk ceramics in seconds", *Science,* **368** [6490] (2020) 521–526.
73. B.W. Zhang, M.C. Hu, F.G. Zhong, S.P. Zhang, Z.W. Yang, X.C. Qiu, J.B. Xu, J. Ou-yang, Y. Zhang, B.P. Zhu, X.F. Yang, S. Chen, "Ultrafast high-temperature sintering and densification of ZrC-based ceramics", *J. Eur. Ceram. Soc.*, **44** [10] (2024) 5569–5578.
74. F.X. Ye, F.W. Meng, T.Y. Luo, H. Qi, "Ultrafast high-temperature sintering of high-entropy $(La_{0.2}Nd_{0.2}Sm_{0.2}Eu_{0.2}Gd_{0.2})_2Hf_2O_7$ ceramics with fluorite structure", *Ceram. Int.*, **48** [23] (2022) 35649–35654.
75. F.X. Ye, F.W. Meng, T.Y. Luo, H. Qi, "Ultrafast high-temperature sintering of $(Y_{0.2}Dy_{0.2}Er_{0.2}Tm_{0.2}Yb_{0.2})_4Hf_3O_{12}$ high-entropy ceramics with defective fluorite structure", *J. Eur. Ceram. Soc.*, **42** [11] (2022) 4686–4691.
76. J. Dong, V. Pouchly, M. Biesuz, V. Tyrpekl, M. Vilémová, M. Kermani, M. Reece, C.F. Hu, S. Grasso, "Thermally-insulated ultra-fast high temperature sintering (UHS) of zirconia: A master sintering curve analysis", *Scr. Mater.*, **203** (2021) 114076.
77. R.F. Guo, H.R. Mao, P. Shen, "Ultra-fast high-temperature synthesis and densification of high-entropy

diborides and diboride-carbide ceramics", *J. Eur. Ceram. Soc.*, **43** [14] (2023) 5763–5773.
78. J.H. Wu, M. Kermani, L. Cao, B.H. Wang, Z.Q. Dai, L. Fu, C.F. Hu, S. Grasso, "Rapid crystallization of $Li_{1.5}Al_{0.5}Ge_{1.5}(PO_4)_3$ glass ceramics via ultra-fast high-temperature sintering (UHS)", *Int. J. Appl. Ceram. Technol.*, **20** [4] (2023) 2125–2130.
79. L.A. Gao, H.Z. Wang, J.S. Hong, H. Miyamoto, S.D. De la Torre, "SiC-Al_2O_3 nanocomposites superfast densified by SPS", *J. Inorg. Mater.*, **14** [1] (1999) 55–60.
80. S. Sovizi, M.E. Seraji, "The densification behavior of metals and alloys during spark plasma sintering: A mini-review", *Sci. Sintering*, **51** [2] (2019) 135–152.
81. X.Y. Li, Z.H. Zhang, X.W. Cheng, G.J. Huo, S.Z. Zhang, Q. Song, "The development and application of spark plasma sintering technique in advanced metal structure materials: A review", *Powder Metall. Met. Ceram.*, **60** [7-8] (2021) 410–438.
82. Z.L. Liao, Q.L. He, W. Zhang, F. Zhang, W.M. Wang, Z.Y. Fu, "B_4C ceramics with increased dislocation density fabricated by reactive spark plasma sintering via carbon nanotubes-boron mixture", *Ceram. Int.*, **50** [13] (2024) 22443–22455.
83. Y. L. Liu, M.D. Yi, Q. Li, Y.J. Song, H. Chen, X.L. Bai, J.J. Zhang, G.C. Xiao, Z.Q. Chen, C.H. Xu, "Low-temperature sintering mechanization of high-entropy (W,Nb,Mo,Ta,Ti)C cermet via spark plasma coupled high-frequency induction sintering", *Ceram. Int.*, **50** [9] (2024) 14936–14947.
84. Z.A. Munir, M. Ohyanagi, "Perspectives on the spark plasma sintering process", *J. Mater. Sci.*, **56** [1] (2021) 1–15.
85. Z.Y. Hu, Z.H. Zhang, X.W. Cheng, F.C. Wang, Y.F. Zhang, S.L. Li, "A review of multi-physical fields induced phenomena and effects in spark plasma sintering: Fundamentals and applications", *Mater. Des.*, **191** (2020) 108662.
86. Z.H. Zhang, Z.F. Liu, J.F. Lu, X.B. Shen, F.C. Wang, Y.D. Wang, "The sintering mechanism in spark plasma sintering - Proof of the occurrence of spark discharge", *Scr. Mater.*, 81 (2014) 56–59.
87. Z.Y. Tan, Z. Xie, X. Wu, J. Guo, W. Zhu, "Spark plasma sintering of $A_6B_2O_{17}$ (A=Hf, Zr; B=Ta, Nb) high entropy ceramics", *Mater. Lett.*, **330** (2023) 133381.
88. Z. Teng, P. Wang, S.F. Zeng, W.L. Feng, C. Chen, P. Jia, Y.Q. Tan, S. Peng, "Reactive spark plasma sintering of high-entropy $(La_{1/7}Nd_{1/7}Sm_{1/7}Eu_{1/7}Gd_{1/7}Dy_{1/7}Ho_{1/7})_2Zr_2O_7$ pyrochlore ceramic", *Ceram. Int.*, **50** [4] (2024) 6892–6897.
89. M. Cologna, B. Rashkova, R. Raj, "Flash sintering of nanograin zirconia in <5 s at 850 °C", *J. Am. Ceram. Soc.*, **93** [11] (2010) 3556–3559.
90. L.A. Perez-Maqueda, E. Gil-Gonzalez, M.A. Wassel, S.K. Jha, A. Perejon, H. Charalambous, J. Okasinski, P.E. Sanchez-Jimenez, T. Tsakalakos, "Insight into the $BiFeO_3$ flash sintering process by in-situ energy dispersive X-ray diffraction (ED-XRD)", *Ceram. Int.*, **45** [2] (2019) 2828–2834.
91. H.R. Mao, R.F. Guo, Y. Cao, S.B. Jin, X.M. Qiu, P. Shen, "Ultrafast densification of high-entropy oxide $(La_{0.2}Nd_{0.2}Sm_{0.2}Eu_{0.2}Gd_{0.2})_2Zr_2O_7$ by reactive flash sintering", *J. Eur. Ceram. Soc.*, **41** [4] (2021) 2855–2860.
92. G.L. Zhao, S.K. Cai, Y. Zhang, H. Gu, C. Xu, "Reactive flash sintering of high-entropy oxide $(La_{0.2}Nd_{0.2}Sm_{0.2}Eu_{0.2}Gd_{0.2})_2Zr_2O_7$: Microstructural evolution and aqueous durability", *J. Eur. Ceram. Soc.*, **43** [6] (2023) 2593–5600.
93. A. Moted, K.Y. Chen, "Modelling and evaluating thermal conductivity of porous thermal barrier coatings at elevated temperatures", *Ceram. Int.*, **46** [14] (2020) 21939–21957.
94. S.T. Masoule, Z. Valefi, N. Ehsani, H.Q. Lavasani, "Thermal insulation and thermal shock behavior of conventional and nanostructured plasma-sprayed TBCs", *J. Therm. Spray Technol.*, **25** [8] (2016) 1684–1691.
95. R. Ghasemi, H. Vakilifard, "Plasma-sprayed nanostructured YSZ thermal barrier coatings: Thermal insulation capability and adhesion strength", *Ceram. Int.*, **43** [12] (2017) 8556–8563.
96. P. Zhang, Y.J. Feng, Y. Li, W. Pan, P.A. Zong, "Thermal and mechanical properties of ferroelastic $RENbO_4$ (RE=Nd, Sm, Gd, Dy, Er, Yb) for thermal barrier coatings", *Scr. Mater.*, **180** (2020) 51–56.
97. R.Z. Zhang, M.J. Reece, "Review of high entropy ceramics: design, synthesis, structure and properties", *J. Mater. Chem. A*, **7** [39] (2019) 22148–22162.
98. J.T. Zhu, X.Y. Meng, P. Zhang, Z.L. Li, J. Xu, M.J. Reece, F. Gao, "Dual-phase rare-earth-zirconate high-entropy ceramics with glass-like thermal conductivity", *J. Eur. Ceram. Soc.*, **41** [4] (2021) 2861–2869.
99. Z.F. Zhao, H. Chen, H.M. Xiang, F.Z. Dai, X.H. Wang, W. Xu, K. Sun, Z.J. Peng, Y.C. Zhou, "$(Y_{0.25}Yb_{0.25}Er_{0.25}Lu_{0.25})_2(Zr_{0.5}Hf_{0.5})_2O_7$: A defective fluorite structured high entropy ceramic with low thermal conductivity and close thermal expansion coefficient to Al_2O_3", *J. Mater. Sci. Technol.*, **39** (2020) 167–172.
100. T. Liu, B. Y. Ma, W.Y. Zan, C. Yu, Z.F. Wang, C.J. Deng, "Green preparation of high entropy ceramics $(Y_{0.2}Sm_{0.2}Eu_{0.2}Er_{0.2}Yb_{0.2})_2SiO_5$ with low thermal conductivity by molten salt synthesis", *Ceram. Int.*, **50** [2] (2024) 2718–2726.
101. D. Song, T. Song, U. Paik, G. Lyu, Y.G. Jung, H.B. Jeon, Y.S. Oh, "Glass-like thermal conductivity in mass-disordered high-entropy $(Y,Yb)_2(Ti,Zr,Hf)_2O_7$ for thermal barrier material", *Mater. Des.*, **210** (2021) 110059.
102. W.W. Sang, W.B. Xie, R.Y. Hou, S.Q. Li, H.S. Zhang, S.X. Liu, X.G. Chen, "Crystal structure and thermophysical properties of $(Gd_{0.25}Sm_{0.25}Yb_{0.25}Y_{0.25})_3TaO_7$ high-entropy oxide", *Ceram. Int.*, **49** [17] (2023) 29358–29363.
103. A.M.F. Dehkharghani, M.R. Rahimipour, M. Zakeri, "Improving the thermal shock resistance and fracture toughness of synthesized $La_2Ce_2O_7$ thermal barrier coatings through formation of $La_2Ce_2O_7$/YSZ composite coating via air plasma spraying", *Surf. Coat. Technol.*, **399** (2020) 126174.
104. J.H. Liu, Z. Lu, Y.W. Zhou, J. Zhang, G.L. Lyu, "A review on the failure behavior and countermeasures of thermal barrier coatings", *J. Ceram. Process. Res.*, **24** [2] (2023) 285–307.
105. Y.H. Chen, R.L. Zhang, G.S. Zhang, P.Y. Jiang, J. Song, X.W. Chu, "Toughening mechanism of thermal barrier coatings", *Int. J. Thermophys.*, **42** [5] (2021) 69.
106. J.T. Zhu, X.Y. Meng, J. Xu, P. Zhang, Z.H. Lou, M.J. Reece, F. Gao, "Ultra-low thermal conductivity and enhanced mechanical properties of high-entropy rare

earth niobates (RE_3NbO_7, RE = Dy, Y, Ho, Er, Yb)", *J. Eur. Ceram. Soc.*, **41** [1] (2021) 1052–1057.
107. X. W. Luo, L. R. Luo, X. F. Zhao, H. Y. Cai, S. S. Duan, C. H. Xu, S. Huang, H. Y. Jin, S. Hou, "Single-phase rare-earth high-entropy zirconates with superior thermal and mechanical properties", *J. Eur. Ceram. Soc.*, **42** [5] (2022) 2391–2399.
108. D.H. Guo, F.F. Zhou, B.S. Xu, Y.G. Wang, Y. Wang, "High-entropy $(La_{0.2}Nd_{0.2}Sm_{0.2}Gd_{0.2}Yb_{0.2})_2(Zr_{0.75}Ce_{0.25})_2O_7$ thermal barrier coating material with significantly enhanced fracture toughness", *Chin. J. Aeronaut.*, **36** [4] (2023) 556–564.
109. C. Vorkötter, D.E. Mack, D.P. Zhou, O. Guillon, R. Vassen, "Effect of low-CTE oxide-dispersion-strengthened bond coats on columnar-structured YSZ coatings", *Coatings*, **12** [3] (2022) 396.
110. J.S. Wang, M.D. Chen, Y.H. Wang, B. Li, Y.S. Yu, Y.S. Tian, B. Liu, Q.S. Jing, "Preparation and thermo-physical properties of La_2AlTaO_7 ceramic for thermal barrier coating application", *Mater. Chem. Phys.*, **289** (2022) 126465.
111. S.Y. Zhang, H.L. Li, S.H. Zhou, T.Q. Pan, "Estimation thermal expansion coefficient from lattice energy for inorganic crystals", *Jpn. J. Appl. Phys.*, **45** [11] (2006) 8801–8804.
112. W.S. Xia, L.X. Li, P.F. Ning, Q.W. Liao, "Relationship between bond ionicity, lattice energy, and microwave dielectric properties of $Zn(Ta_{1-x}Nb_x)_2O_6$ ceramics", *J. Am. Ceram. Soc.*, **95** [8] (2012) 2587-2592.
113. L.G. Van Uitert, H.M. O'Bryan, M.E. Lines, H.J. Guggenheim, G. Zydzik, "Thermal expansion-An empirical correlation", *Mater. Res. Bull.*, **12** [3] (1977) 261–268.
114. H. Vakilifard, H. Shahbazi, A.C. Liberati, R.B.N. Saraswathy, R.S. Lima, M.D. Pugh, C. Moreau, "High entropy oxides as promising materials for thermal barrier topcoats: A review", *J. Therm. Spray Technol.*, **33** [2-3] (2024) 447–470.
115. F. Sun, X.L. Fan, T. Zhang, P. Jiang, J.J. Yang, "Numerical analysis of the influence of pore microstructure on thermal conductivity and Young's modulus of thermal barrier coating", *Ceram. Int.*, **46** [15] (2020) 24326–24332.
116. T. Yang, W.Z. Wang, J.B. Huang, Y.G. Liu, K.B. Li, Z.N. Yang, Y.H. Wang, B.H. Yuan, C.C. Zhang, "Investigation of sintering mechanism for novel composite structural thermal barrier coating", *J. Am. Ceram. Soc.*, **106** [9] (2023) 5541–5558.
117. K. Torkashvand, E. Poursaeidi, J. Ghazanfarian, "Experimental and numerical study of thermal conductivity of plasma-sprayed thermal barrier coatings with random distributions of pores", *Appl. Therm. Eng.*, **137** (2018) 494–503.
118. X.W. Luo, S. Huang, R.Q. Huang, C.H. Xu, S. Hou, H.Y. Jin, "Highly anti-sintering and toughened pyrochlore $(Dy_{0.2}Nd_{0.2}Sm_{0.2}Eu_{0.2}Yb_{0.2})_2Zr_2O_7$ high-entropy ceramic for advanced thermal barrier coatings", *Ceram. Int.*, **49** [4] (2023) 23410–23416.
119. J. Wells, N. Chapman, J. Sumner, P. Walker, "The use of APS thermal barrier coatings in corrosive environments", *Oxid. Met.*, **88** [1] (2017) 97–108.
120. H.L. Chang, C.Y. Cai, Y.G. Wang, Y.C. Zhou, L. Yang, G.W. Zhou, "Calcium-rich CMAS corrosion induced microstructure development of thermal barrier coatings", *Surf. Coat. Technol.*, **324** (2017) 577–584.
121. L. Guo, Y. Gao, Y.X. Cheng, J.Y. Sun, F.X. Ye, L. Wang, "Microstructure design of the laser glazed layer on thermal barrier coatings and its effect on the CMAS corrosion", *Corros. Sci.*, **192** (2021) 109847.
122. T.Z. Tu, J.X. Liu, L. Zhou, Y.C. Liang, G.J. Zhang, "Graceful behavior during CMAS corrosion of a high-entropy rare-earth zirconate for thermal barrier coating material", *J. Eur. Ceram. Soc.*, **42** [2] (2022) 649–657.
123. S.X. Deng, G. He, Z.G. Yang, J.X. Wang, J.T. Li, L. Jiang, "Calcium-magnesium-alumina-silicate (CMAS) resistant high entropy ceramic $(Y_{0.2}Gd_{0.2}Er_{0.2}Yb_{0.2}Lu_{0.2})_2Zr_2O_7$ for thermal barrier coatings", *J. Mater. Sci. Technol.*, **107** (2022) 259–265.
124. F.X. Ye, F.W. Meng, T.Y. Luo, H. Qi, "The CMAS corrosion behavior of high-entropy $(Y_{0.2}Dy_{0.2}Er_{0.2}Tm_{0.2}Yb_{0.2})_4Hf_3O_{12}$ hafnate material prepared by ultrafast high-temperature sintering (UHS)", *J. Eur. Ceram. Soc.*, **43** [5] (2023) 2185–2195.
125. M. Bahamirian, S.M.M. Hadavi, M. Farvizi, M.R. Rahimipour, A. Keyvani, "Enhancement of hot corrosion resistance of thermal barrier coatings by using nanostructured $Gd_2Zr_2O_7$ coating", *Surf. Coat. Technol.*, **360** (2019) 1–12.
126. Z.J. Fan, K.D. Wang, X. Dong, R.J. Wang, W.Q. Duan, X.S. Mei, W.J. Wang, J.L. Cui, S. Zhang, C.Y. Xu, "The role of the surface morphology and segmented cracks on the damage forms of laser re-melted thermal barrier coatings in presence of a molten salt (Na_2SO_4+V_2O_5)", *Corros. Sci.*, **115** (2017) 56–67.
127. L. Guo, C.L. Zhang, M.Z. Li, W. Sun, Z.Y. Zhang, F.X. Ye, "Hot corrosion evaluation of Gd_2O_3-Yb_2O_3 co-doped Y_2O_3 stabilized ZrO_2 thermal barrier oxides exposed to Na_2SO_4+V_2O_5 molten salt", *Ceram. Int.*, **43** [2] (2017) 2780–2785.
128. G. Azimi, R. Dhiman, H.M. Kwon, A.T. Paxson, K.K. Varanasi, "Hydrophobicity of rare-earth oxide ceramics", *Nat. Mater.*, **12** [4] (2013) 315–320.
129. D. Song, T. Song, U. Paik, G. Lyu, J. Kim, S. Yang, Y.G. Jung, "Hot-corrosion resistance and phase stability of Yb_2O_3-Gd_2O_3-Y_2O_3 costabilized zirconia-based thermal barrier coatings against Na_2SO_4+V_2O_5 molten salts", *Surf. Coat. Technol.*, **400** (2020) 126197.
130. G. Roncallo, E. Barbareschi, G. Cacciamani, E. Vacchieri, "Effect of cooling rate on phase transformation in 6-8 wt% YSZ APS TBCs", *Surf. Coat. Technol.*, 412 (2021) 127071.
131. Y.C. Wu, Y.T. Chiang, "The m-t transformation and twinning analysis of hot-pressed sintered 3YSZ ceramics", *J. Am. Ceram. Soc.*, **94** [7] (2011) 2200–2212.
132. S. Wu, Y.T. Zhao, W.G. Li, W.L. Liu, Y.P. Wu, Z.X. Zhao, "Na_2SO_4+NaCl molten salts corrosion mechanism of thermal barrier coatings used in ships", *J. Therm. Anal. Calorim.*, **144** [6] (2021) 2043–2056.
133. H.L. Zhu, L. Liu, H.M. Xiang, F.Z. Dai, X.H. Wang, Z. Ma, Y.B. Liu, Y.C. Zhou, "Improved thermal stability and infrared emissivity of high-entropy $REMgAl_{11}O_{19}$ and $LaMAl_{11}O_{19}$ (RE = La, Nd, Gd, Sm, Pr, Dy; M=Mg, Fe, Co, Ni, Zn)", *J. Mater. Sci. Technol.*, **104** (2022) 131–144.
134. R.X. Liu, W.P. Liang, Q. Miao, H. Zhao, S. Ramakrishna, B. Ramasubramanian, X.F. Zhang, Y.D. Song, X.G. Gao, J.K. Du, X.M. Tao, "A novel defect

fluorite type high-entropy $(Dy_{0.2}Ho_{0.2}Er_{0.2}Tm_{0.2}Lu_{0.2})_2Hf_2O_7$ ceramic with low thermal conductivity and CTE: a mechanism study", *J. Mater*. *Res*. *Technol*., **27** (2023) 1365–1380.

135. L.K. Cong, W. Li, J.C. Wang, S.Y. Gu, S.Y. Zhang, "High-entropy $(Y_{0.2}Gd_{0.2}Dy_{0.2}Er_{0.2}Yb_{0.2})_2Hf_2O_7$ ceramic: A promising thermal barrier coating material", J. *Mater*. *Sci*. *Technol*., **101** (2022) 199–204.